



UNIVERSITY OF BERGAMO
DEPARTMENT OF ENGINEERING AND APPLIED SCIENCES
DOCTORAL PROGRAM IN ENGINEERING AND APPLIED SCIENCES

DEVELOPMENT AND INVESTIGATION OF INNOVATIVE MATERIALS PRODUCED BY MEANS OF ADDITIVE MANUFACTURING TECHNOLOGIES

Tutor:

Prof. Tommaso Pastore – University of Bergamo
Ing. Giuseppe Barbieri - ENEA

Doctoral dissertation of:
Francesco Carugo

XXXV Cycle

ABSTRACT

Nickel-based alloys are widely used in industries characterized by harsh operating environments such as chemical, aerospace, nuclear, and oil and gas. Among these, nickel alloy 625 plays a strategic role, especially in the oil and gas sector, due to its high mechanical properties combined with exceptional corrosion resistance.

The work-hardened austenitic matrix, however, makes it difficult to be machined by conventional machining technologies. In this context, the spread of additive manufacturing (AM) technologies applied to metals has been gaining increasing interest in the industrial world in recent years. These techniques, based on a layer-by-layer approach, allow design strategies to be redefined, enabling the creation of complex-shaped components, optimizing geometry and in some cases reducing costs.

Among the AM techniques available today, the most popular are powder bed-based techniques such as Laser Powder Bed Fusion (LPBF) and Directed Energy Deposition (DED) techniques. Recently, new techniques are being developed that combine the printing process with debinding and sintering processes. Among these, Metal Fused Filament Fabrication (MFFF) is an emerging technique that uses a filament composed of metal powder and polymer to make a component. The component thus made is then subjected to a debinding cycle, to remove the polymer, followed by a sintering treatment to densify the final product.

Depending on the AM technique used, completely different microstructures from traditional ones are obtained. Therefore, the issue related to the qualification of these new materials becomes fundamental, especially if they are intended for use in environments characterized by severe operating conditions.

The purpose of this thesis is to evaluate the corrosion behavior of nickel alloy 625 obtained by means of three different additive manufacturing technologies: the LPBF, the DED and the MFFF techniques. Specifically, corrosion behavior was evaluated by comparing the results obtained with those of a commercial product produced by hot rolling. Regarding the MFFF and DED technique, the effect of post-process hot isostatic pressing on corrosion behavior was evaluated in relation to the characteristic microstructures obtained.

Contents

1 INTRODUCTION.....	1
2 ADDITIVE MANUFACTURING TECHNOLOGIES	3
2.1 Laser Powder Bed Fusion process.....	5
2.2 Directed Energy Deposition.....	7
2.3 Metal Fused Filament Fabrication.....	8
2.4 Material feedstock for AM processes	9
3 CHARACTERISTICS OF AM TECHNOLOGIES	11
3.1 Defects	11
3.2 Microstructures	12
3.3 Post-processing treatments	13
4 CORROSION BEHAVIOR OF NICKEL ALLOY.....	15
4.1 Generalized corrosion	15
4.2 Localized corrosion.....	16
4.3 Intergranular corrosion.....	18
4.4 Effect of AM technologies on corrosion behavior	20
5 EXPERIMENTAL METHODOLOGY.....	23
5.1 Feedstock materials	23
5.2 Specimens	25
5.3 Post process heat treatment	28
5.4 Metallographic analysis	29
5.5 Intergranular corrosion tests	30
5.6 Potentiodynamic polarization tests.....	31
5.7 Potentiostatic polarization tests	32
5.8 Hardness tests	32

6 RESULTS	33
6.1 DED process parameters optimization	33
6.2 Porosity analysis	36
6.3 Microstructural analysis	38
6.4 Intergranular corrosion tests	43
6.5 Potentiodynamic polarization tests.....	44
6.6 Potentiostatic polarization tests	51
6.7 Hardness tests	58
7 DISCUSSION	61
7.1 Defect analysis on MFFF-manufactured specimens.....	61
7.2 Selective corrosion behavior.....	64
7.1 Localized corrosion behavior	66
8 CONCLUSION.....	73
REFERENCES	75

List of figures

Figure 2-1: Schematic diagram of LPBF process [41]	6
Figure 2-2: Example of scanning strategy used in LPBF process [48].....	7
Figure 2-3: Schematic representation of a DED system. a) powder DED system, b) wire DED system [59]	8
Figure 2-4: Schematic diagram of MFFF process [61]	9
Figure 2-5: Schematic representation of the atomization process. a) gas atomization process, b) plasma rotating electrode process [66]	10
Figure 3-1: Rough surface caused by approximation of curve surface[69]..	12
Figure 4-1: Iso-corrosion curves of nickel alloy in H_2SO_4 solutions.....	16
Figure 4-2: Iso-corrosion curves of nickel alloys in HCl containing solutions	16
Figure 4-3: Corrosion behavior in SO_2	17
Figure 4-4: TTT diagram of Alloy 625	19
Figure 5-1: Schematic representation of the scanning strategy adopted for the MFFF-manufactured specimens	25
Figure 5-2:DED-manufactured thin wall.....	28
Figure 5-3: Temperature and pressure versus time during the HIP process performed.....	29
Figure 6-1: Morphological appearance of some of the specimens made for the optimization of DED process parameters. a) D15, b) D11 and c) D5.....	33
Figure 6-2:Example of defects observed on the micrographs of the cross section. a) macro pore on D8 specimen, b) crack on D1 specimen.....	35
Figure 6-3: Mean value and standard deviation of Vickers hardness of process parameter optimization specimens D1 to D15	35

Figure 6-4: metallographic cross-section (45 ° cut) of a MFFF-produced sample with different types of defects highlighted.....	38
Figure 6-5: Optical microscopy images of the microstructure of the a) LPBF-, b) DED-, c) MFFF-manufactured and d) HW specimens.....	39
Figure 6-6: SEM images of the microstructure of the a) LPBF-, b) DED-, c) MFFF-manufactured and d) HW specimens.....	41
Figure 6-7: EDS map analysis covering an oxide inclusion found in the MFFF-manufactured alloy 625	42
Figure 6-8: EDS map a) performed on MFFF-processed specimen and b) relative comparison of the diffraction pattern of the secondary phases found and the matrix	43
Figure 6-9: Different response during the susceptibility to intergranular corrosion test. a) DED-processed specimen b) core region of the MFFF-processed material c) contour region of the MFFF-processed material	44
Figure 6-10: Potentiodynamic polarization curves in 1N H ₂ SO ₄ solution: a) LPBF-, b) MFFF-, c) DED-manufactured samples and, d) HW sample	46
Figure 6-11: Potentiodynamic polarization curves in 0.6 M NaCl at pH 7: a) LPBF-, b) MFFF-, c) DED-manufactured samples and, d) HW sample	48
Figure 6-12: Potentiodynamic polarization curves in 0.6 M NaCl at pH 3: a) LPBF-, b) MFFF-, c) DED-manufactured samples and, d) HW sample	50
Figure 6-13: Crevice corrosion on MFFF UT specimen. a) Optical microscopy image, b) SEM image.....	51
Figure 6-14: Current density vs. time during potentiostatic tests conducted on LPBF specimens a) at + 200 mV vs. SCE in 0.6M NaCl at pH7 b)) at + 500 mV vs. SCE in 0.6M NaCl at pH7 c)) at + 200 mV vs. SCE in 0.6M NaCl at pH3 d)) at + 500 mV vs. SCE in 0.6M NaCl at pH3	52
Figure 6-15: Current density vs. time during potentiostatic tests conducted on MFFF specimens a) at + 200 mV vs. SCE in 0.6M NaCl at pH7 b)) at + 500	

mV vs. SCE in 0.6M NaCl at pH7 c)) at + 200 mV vs. SCE in 0.6M NaCl at pH3 d)) at + 500 mV vs. SCE in 0.6M NaCl at pH3	55
Figure 6-16: Current density vs. time during potentiostatic tests conducted on DED specimens a) at + 200 mV vs. SCE in 0.6M NaCl at pH7 b)) at + 500 mV vs. SCE in 0.6M NaCl at pH7 c)) at + 200 mV vs. SCE in 0.6M NaCl at pH3 d)) at + 500 mV vs. SCE in 0.6M NaCl at pH3	58
Figure 6-17: Outcome of the low force Vickers hardness test for the AM- processed specimens.....	59
Figure 7-1: Representative view of the wire scan directions and their correspondence with the locations of a),b) the triangular macro-defects in the core and c)quadrilateral macro-defects in the contour). The green, blue, and orange dashed lines represent respectively the parallel, perpendicular, and 45°- oriented wire scan lines, with respect to the cross-section plane. The sizes represented were altered on purpose to improve the readability	62
Figure 7-2: a) Pore size distribution and b) pore aspect ratio distribution and correlation with size by image analysis of the optical micrographs of the MFFF- processed samples.....	64
Figure 7-3: Different microstructural features in the microstructure (a,b) and inside the elongated macro-defects (c,d) in the core and contour of the MFFF-produced alloy 625, respectively.....	65
Figure 7-4: E_{corr} of Alloy 625 obtained by means of AM and traditional technology in different test solutions	66
Figure 7-5:Transpassive potential (E_t) as a function of pH for a) AM-fabricate specimens in untreated conditions and b) AM-manufactured specimen after post-processing treatment compared with the HW.....	68
Figure 7-6: Corrosion current density as a function of pH for a) AM-fabricate specimens in untreated conditions and b) AM-manufactured specimen after post-processing treatment compared with the HW.....	69

Figure 7-7: Corrosion current density in the passive range as a function of pH
for a) AM-fabricate specimens in untreated conditions and b) AM-manufactured specimen after post-processing treatment compared with the HW 70

List of tables

Table 1-1: Chemical requirement for Alloy 625 according to ASTM B443 [13].1	
Table 5-1: Composition of the feedstock materials used	24
Table 5-2: Different process parameters used for DED-manufactured samples.....	27
Table 6-1: Cross-section thickness of process parameter optimization specimens D1 to D15	34
Table 6-2: Characteristics of the process parameters optimization	36
Table 6-3: Porosity and relative fraction of pores > 50 µm.....	37
Table 6-4: Corrosion rates evaluated according to ASTM G28 method A [89]. The data relative to the LPBF-produced and HW specimens come from a previous publication [84].....	43

INTRODUCTION

Nickel superalloys possess high mechanical and corrosion resistance properties even at elevated temperatures [1,2]. Among them, Alloy 625, also known as Inconel 625, is a Ni-Cr-Mo alloy that is the main choice for applications characterized by particularly aggressive operating environments, such as the oil and gas industry, chemical, nuclear, and aerospace applications [3–11]. The popularity of this material is mainly due to its excellent combination of mechanical properties, weldability, thermal stability, as well as high creep, oxidation, and corrosion resistances in host solutions [12]. The reference chemical composition according to ASTM B443 [13] is given in Table 1-1:

Table 1-1: Chemical requirement for Alloy 625 according to ASTM B443 [13].

	Ni	Cr	Mo	Fe	Nb+Ta	Co	Mn	Si	Al	Ti	C	P	S
wt	58.0	20.–	8.0–	5.0	3.15–	1.0	0.50	0.50	0.40	0.40	0.10	0.015	0.015
%	min	23.0	10.0	max	4.15	max	max	max	max	max	max	max	max

Alloy 625 is a solid solution strengthened superalloy characterized by a face-centered cubic austenitic structure (γ phase). The strengthening mechanism is related to the addition of elements with high solubility such as Nb and Mo [14] which, due to a larger size than the nickel atom, deform the crystal lattice structure and inhibit the movement of dislocations.

High mechanical strength is due to the presence of second phases that can precipitate within the austenitic matrix. The most important is the γ' phase of $\text{Ni}_3(\text{Al},\text{Ti})$ composition characterized by a face-centered cubic structure and generally dispersed within the γ matrix. The morphology with which it occurs is strongly influenced by the heat treatments and chemical composition and can be in spherical form for maximum lattice distortions between γ' and γ of 0.2 %, cuboidal for lattice distortions between 0.5 % and 1 %, while it takes a platelet form for distortions greater than 1.25 % [15,16].

γ'' phase of Ni_3Nb characterized by a body-centered tetragonal structure can also be found in the alloy. This phase, when the alloy is exposed to temperatures above 650 °C for a prolonged period, turns into the orthorhombic structure phase, more stable thermodynamically, but which leads to a significant deterioration of mechanical properties[17]. Hardening effect by γ'' is therefore effective only at low temperatures.

Alloy 625 also contains carbides of the form MC , M_6C and M_{23}C_6 . These carbides can be classified as primary or secondary, depending on whether they are formed during solidification in the manufacturing process or after exposure to high temperatures respectively.

The alloy 625 is typically processed using conventional manufacturing technologies, such as casting or forging. However, these techniques are usually related to a low degree of material usage. In addition, the possibility to generate complex-shaped components is somehow limited. Therefore, the investigation of new manufacturing technologies to overcome these issues is industrially very relevant [18]. In this context, Additive Manufacturing (AM) technologies are becoming a consolidated reality for nickel alloys production in recent years.

ADDITIVE MANUFACTURING TECHNOLOGIES

In recent years, the industrial panorama has been evolving rapidly, and a revolution driven by technologies capable of redefining traditional methods of producing materials and products is being observed. From an engineering perspective, among the classes of materials involved in this revolution, metals are gaining increasing prominence. In fact, the rapid growth of AM technologies, has introduced new trends in the field of manufacturing technologies and development of new materials, due to the significant advantages of these techniques [19,20].

AM is based on a layer-by-layer approach to build a component from a 3D CAD model that is divided into 2D sections [21–23]. This allows for the fabrication of components of even very complex geometries [24] that cannot be achieved through traditional machining techniques by material removal. In addition, the extreme design flexibility can lead to a reduction in the number of parts produced, eliminating the need to assemble multiple components.

However, given the high costs of printers and production time, AM techniques are not particularly attractive to the industrial sector and their massive market penetration is still limited, although their potential is

Chapter 2

Additive manufacturing technologies

significant. In this context, it seems more strategic to focus on materials and solutions with high added value that, due to their specificity, can find in additive technology a unique and strategic solution, not limited only to the economic aspect. Among the available metal alloys, certainly those with high mechanical performance and corrosion resistance, such as nickel-based superalloys, appear most significant. These materials are also characterized by high hardness and low thermal diffusivity, which in some cases makes their processing by traditional techniques particularly difficult and expensive.

Currently, several metal AM technologies are available in the market that can be distinguished according to several factor, such as the feedstock material form (powder, wire) or the absence/presence of a polymeric binder. The more widespread and established are Powder Bed Fusion (PBF) and Directed Energy Deposition (DED) technologies.

Laser Powder Bed Fusion (LPBF) machines selectively melt prealloyed particles in a powder bed using a laser as a heat source. When the layer is completed, a new one is spread over the previous one and the process continues until the 3D component is built. This technology is very consolidated on an industrial level and grants high dimensional accuracy and the possibility to build complex parts (e.g., thin walls, hollow channels) [25–27].

Conversely, in Directed Energy Deposition (DED) systems, the feedstock material can be either in the form of powder or wire. In both scenarios, it is directly delivered onto the melting area and melted by a laser. The build-up rates achieved are significantly higher with respect to powder bed systems. Moreover, DED can be adopted for gradient composition production and repairing/remanufacturing operations [28–30].

Metal Fused Filament Fabrication (MFFF) is a rather new commercially available AM technology, which implies the fusion of a polymeric filament filled with metal particles, generating a green part. This is subsequently

debinded to remove the polymer and then sintered at high temperature, to achieve high densities. MFFF-manufactured parts are usually characterized by lower dimensional accuracy and strength with respect to most of the other AM technologies [31,32]. This is generally linked to a lower density achieved in the final component. Notwithstanding that, the process time and the relative costs are greatly reduced [33].

2.1 Laser Powder Bed Fusion process

LPBF is one of the leading powder-based additive manufacturing technologies with which nickel alloy components are fabricated [34–36]. Depending on the 3D printer manufacturer, this technology is also known as Direct Metal Laser Sintering (DMLS), Selective Laser Melting (SLM) or Selective Laser Sintering (SLS) [37–39].

A typical schematic of an LPBF process is shown in Figure 2-1. The entire process of making a component takes place in a closed chamber and in an atmosphere protected by inert gas, typically Ar or N₂, to avoid oxidation and powder degradation. The main steps of single-layer fabrication are [40]:

- A recoater system, typically consisting of a blade or cylinder, moves from the dispenser chamber to the build platform distributing a uniform layer of powder one layer thick.
- Once the powder has been deposited, the laser beam guided by a mirror optical system goes to fuse a single layer of powder according to the CAD data.
- After completing the layer, the construction platform is lowered by an amount equal to the thickness of the layer just realized.
- At the same time, the recoater returns to its starting position and the dispenser platform moves upward so that a new layer of powder can be deposited.
- The process is repeated until completion and finally the part is removed from the powder bed.

Chapter 2

Additive manufacturing technologies

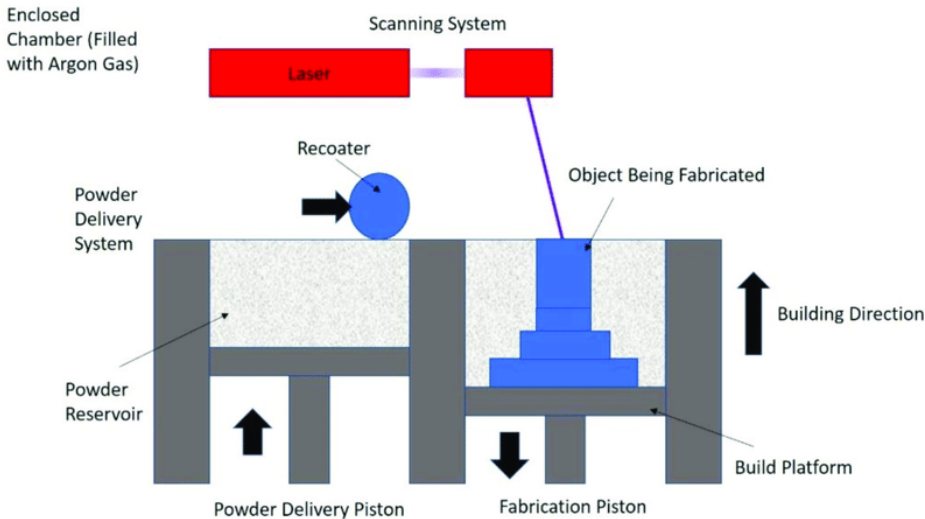


Figure 2-1: Schematic diagram of LPBF process [41].

Powders, as well as the building platform, can be preheated in order to avoid excessive temperature gradients during the powder melting process. In addition, this preheating allows to use less laser power and helps to reduce deformation due to non-uniform thermal expansion and contraction, thus improving the quality of the final product [42].

The most important process parameters for LPBF technology are the power of the laser P , the laser scanning speed, the layer thickness and the hatching distance h_d , that is the distance between two consecutive laser scans. In the literature these parameters are combined in the density of volumetric energy E_D , expressed by the following relationship [43–47]

$$E_D = \frac{P}{v \cdot h_D \cdot t} \quad \text{Eq. 2-1}$$

As E_D changes, the characteristics of the realized component change.

Another important parameter in the LPBF process is the scanning strategy, which is the movement that the laser beam makes to generate the single slice of the component. Some examples are given in Figure 2-2.

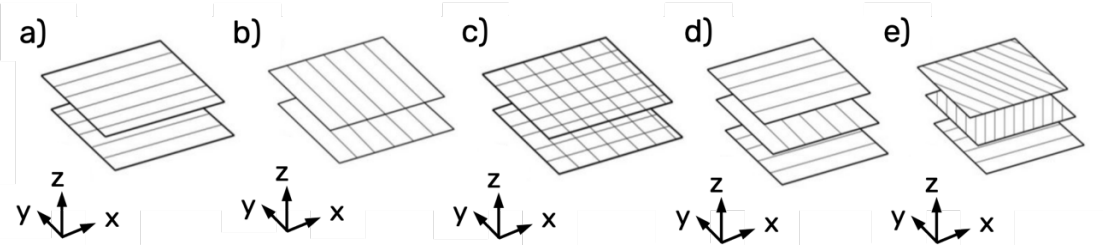


Figure 2-2: Example of scanning strategy used in LPBF process [48].

The scanning area can be divided into square areas or stripes[48]. In the first case (Figure 2-2c), square areas can be scanned according to a precise scheme or randomly [49–51]. In the second case, between successive layers the stripes can be oriented along the x or y direction (Figure 2-2a and b) or alternately (Figure 2-2 d). As reported by several authors in the literature [52–55] the scanning strategy introduced by EOS that involves the rotation of the stripes of 67° years between successive layers (Figure 2-2e) allows to reduce the anisotropy of the component in the x-y plane.

2.2 Directed Energy Deposition

DED is another AM technology with which more nickel-based alloy components are manufactured [56,57]. As with LPBF technology, depending on the printer manufacturer, this technology is also known as Laser Engineered Net Shaping (LENS), Direct Metal Deposition (DMD) or Wire Arc Additive Manufacturing (WAAM) [58].

In DED systems, unlike powder-bed based systems, the raw material is deposited on a substrate where a high-power density energy source such as a laser, electron beam or plasma is focused. Then the raw material, which can be in the form of wire or powder, is melted as it is deposited. During the process an inert gas is used to prevent oxidation of the deposit during solidification and in the case that the source is an electron beam, the process must be performed under vacuum. Figure 2-3 shows schematic representations of a deposition head of a powder DED system (Figure 2-3a) and a wire system (Figure 2-3b).

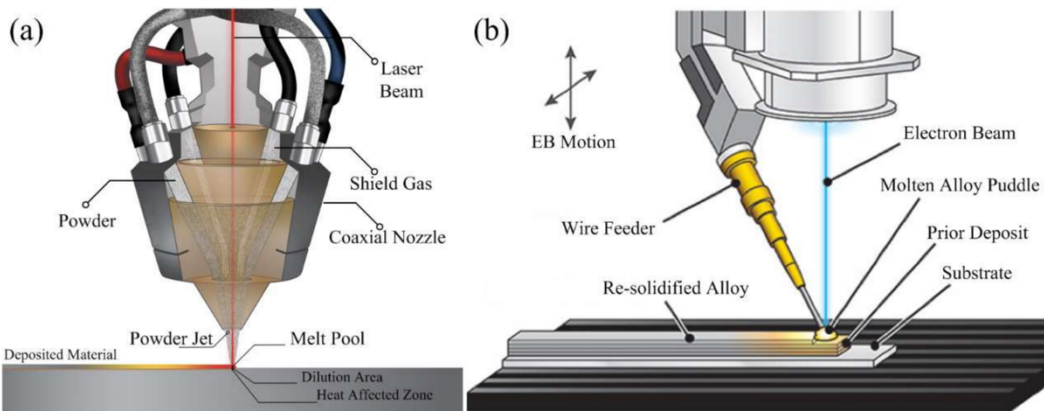


Figure 2-3: Schematic representation of a DED system. a) powder DED system, b) wire DED system [59].

Wire systems are generally less accurate than powder systems because the wire has a fixed shape. However, they are more efficient from the point of view of raw material consumption as all the material is used to create the layer.

One of the advantages associated with DED technology is the ability to deposit multiple materials simultaneously. In addition, some systems use a deposition head mounted on a multi-axial handling system that allows depositing material in multiple directions. For this reason, this technique is often used to repair objects, such as turbine blades, or to make metal coatings.

2.3 Metal Fused Filament Fabrication

Nowadays, AM techniques using a filament made of polymer-bonded metal powder are gaining considerable interest due to the possibility of revolutionizing the way metal components are manufactured [60].

MFFF processes are based on a totally different approach from LPBF and DED systems and are a less expensive alternative. Unlike powder or wire fusion technologies, the printing step does not make use of high-power energy sources and high material temperature gradients are absent. In this case, the metal powder is combined with a thermoplastic polymer powder (binder) to form a filament. To achieve high density values after the sintering process, it

is required that the metal powder content is between 50 and 60 % vol [61]. Figure 2-4 shows a schematic diagram of a MFFF printing step: a feeding system adds the filament into the processing zone with a plunger system, which allows it to be extruded through a nozzle.

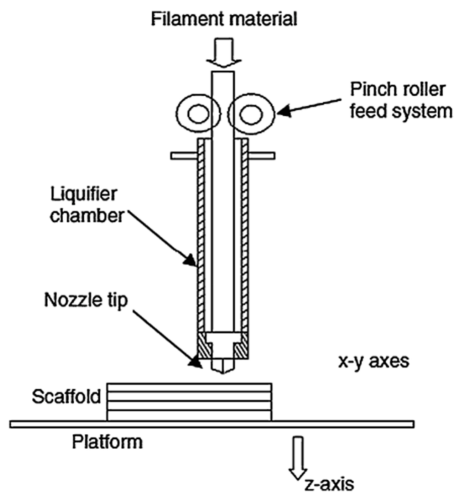


Figure 2-4: Schematic diagram of MFFF printing phase [62].

The green part is then subjected to the process of removing the polymer component. depending on the binder used, the debinding process can be chemical (solvent debinding) or thermal (thermal debinding). Finally, during sintering process in inert gas at high temperatures, metal particles fuse together due to diffusion mechanisms, yielding dense metallic structures [61].

2.4 Material feedstock for AM processes

The quality of the AM-produced part strongly depends on the quality of the feedstock material used.

For processes based on the use of powders as feedstock material, the morphology, size distribution, composition, flowability and surface conditions are among the characteristics that most affect the quality of the additive manufactured components [63,64]. Some authors reports that LPBF powders have size around 10 - 63 μm while DED powders have size around 45 - 150 μm [65,66].

Powder quality is closely related to production technology. the main methods by which powder particles are obtained for additive applications are the gas atomization (Figure 2-5a) the plasma rotating electrode process (Figure 2-5b), the rotary atomization and the water atomization.

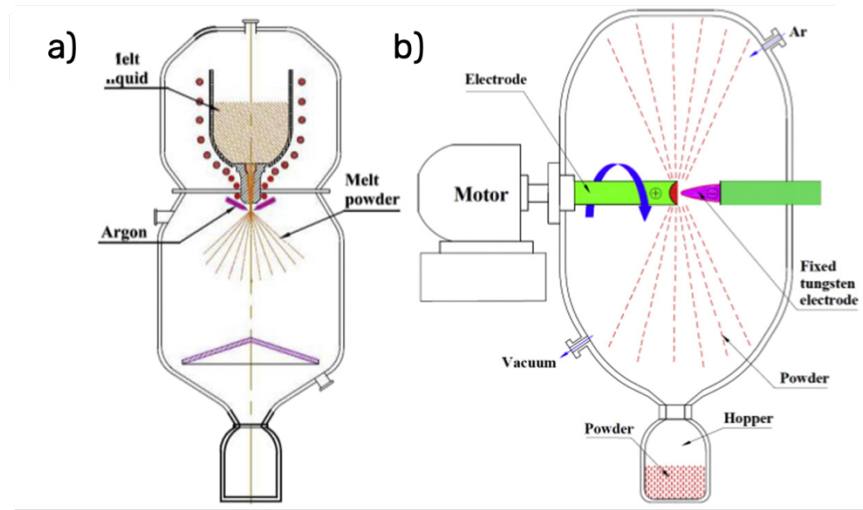


Figure 2-5: Schematic representation of the atomization process. a) gas atomization process, b) plasma rotating electrode process [67].

The first method involves the atomization of the molten alloy by a high-pressure gas flow, typically argon or nitrogen. This gas, during solidification of the particle can become trapped, causing porosity. Through gas atomization, it is possible to obtain powders with spherical morphology, but with the presence of satellite particles that lead to increased surface roughness. In the plasma rotating electrode process a metal bar is melted during rotation. The molten metal is then atomized in the form of droplets that solidify in an inert gas atmosphere to prevent oxidation. Powder particles collected by centrifugal force are characterized by a spherical morphology without defects. In the rotary atomization process, molten alloy is deposited on a rotating disc that throws the molten metal droplets toward the perimeter of the atomization chamber. The solidified powder particles are irregular and are not spherical. In water atomization process high pressure water jet is used to atomize and solidify the liquid metal droplets as powders. The resulting powder particles are usually irregularly shaped with lower fluidity.

CHARACTERISTICS OF AM TECHNOLOGIES

3.1 Defects

AM-produced components are characterized by defects that are related to the technique used and therefore to characteristic process parameters.

Although many efforts have been made in recent years to optimize the process parameters of AM techniques, porosity remains one of the aspects that strongly affects mechanical behavior and it is very important to minimize this phenomenon which is common in all AM processes [68,69]. The factors that lead to an increase in porosity in additive components are many, such as, for example, for powder bed-based processes, the quality of the raw material, and in particular the morphology and grain size. Moreover, in processes that use an energy source to melt the material, if during the process excessive power is used, the melting zone can become unstable and cause a collapse by leaving a pore.

Another characteristic defect of AM technologies is surface roughness. The process parameters used in the printing phase can significantly change the final appearance of the material. Post-processing treatments such as surface machining, grinding, chemical polishing and shot peening are often

required as low roughness is required. The roughness is also due to the "step effect", that is, the approximation of curved surfaces as shown Figure 3-1. Therefore, the balance between the precision required by the component and the production cycle time is a major point during the set of printing parameters. Small deposition thickness for single layer greatly reduces surface roughness, but it takes longer to build the same volume[70].

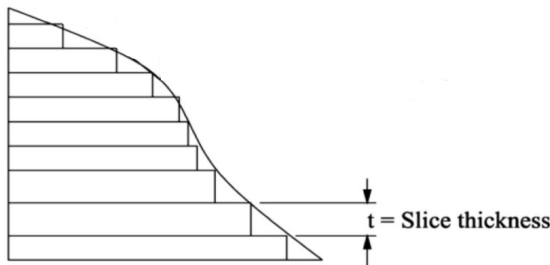


Figure 3-1: Rough surface caused by approximation of curve surface [70].

Components made using LPBF and DED techniques can be subjected to cracks due to the high thermal gradients during the deposition phase of the material. In fact, the material is subject to continuous heating and cooling cycles that cause internal stresses. Moreover, in the partially melted zone the second phases can precipitate inducing a tensile force due to the retreat of the solidification and the thermal contraction during the cooling [71]. Some materials such as nickel superalloy are prone to this type of crack [72].

Residual stresses do not implicate only cracks but also distortion, bad tolerance, low fatigue, and fracture resistance [73,74].

3.2 Microstructures

The microstructure of the materials obtained through AM techniques is completely different from those of the same materials obtained through traditional processing techniques. Moreover, the microstructure also depends on the additive process used and therefore on the thermal history to which the material is subject.

In the LPBF process, the laser beam fuses layers of powder, generating a microstructure characterized by melt pools. Shape and arrangement of melt

pools depend on the scanning strategy used. As reported by Marchese, during the deposition process, heat is dissipated mainly along the building direction, generating anisotropy and the formation of columnar grains [75]. In the direction perpendicular to the building direction, on the other hand, the microstructure is characterized by randomly oriented equiaxial grains. It is possible to notice the presence of two different types of very thin dendritic structures inside the melt pool. The morphology of the first structure is elongated along the building direction along the heat flow, while the second is characterized by a cellular form. These microstructures derive from the high cooling rate, usually higher than 103 K/s and their dimensions can be smaller than 1, 5 μm .

The characteristic microstructure of materials obtained by means of DED technique is similar to that of LPBF and consists of columnar grains along the building direction with a larger dendritic structure due to the cooling rates that are lower respect to the LPBF.

3.3 Post-processing treatments

In many cases, after the manufacturing process of components using AM techniques, it is often necessary to carry out appropriate heat treatments to increase material performance by modifying the microstructure and to reduce internal stresses (relieving stress treatment) related to production conditions. Homogenization heat treatments are mainly necessary for re-dissolving the second undesirable phases and for producing materials and parts with predictable and reproducible properties [76]. However, such heat treatments can affect mechanical properties due to unwanted growth of grain size, which directly affect hardness, yield strength, tensile strength, the fatigue strength, and toughness of these alloys. It is therefore necessary to have a complete understanding of the effects of heat treatment on the microstructure and on the evolution of the different phases present in the material produced by AM.

Chapter 3

Characteristics of AM technologies

Hot Isostatic Pressing (HIP) or heat treatment are used to minimize the residual stress and change/homogenize the microstructure. Traditional heat treatment developed for the specific metal alloy being employed are commonly used. However, special heat treatment methods have been studied to maintain the fine-grained microstructure within the AM part in order to retain high mechanical properties. The HIP process combines high temperature and isostatic inert gas pressure in a high-pressure containment vessel. Heat and pressure, applied simultaneously, can eliminate internal voids and residual stresses resulting in a very fine-grained structure [77].

CORROSION BEHAVIOR OF NICKEL ALLOY

4.1 Generalized corrosion

Generalized corrosion manifests as a uniformly distributed attack on the metal surface. Nickel alloys containing chromium develop a stable and protective homogeneous oxide layer that makes them resistant in many operating environments. Alloy 625 exhibits exceptional corrosion resistance even in marine environments, with estimated average corrosion rates of less than 0.05 mm/year.

Figure 4-1 shows that in sulfuric acid, Inconel 625 has a corrosion rate of less than 0.5 mm/year at temperatures below 35°C, regardless of H₂SO₄ concentration, outperforming AISI 316. In superalloys with molybdenum contents between 27% and 33% regardless of sulfuric acid concentration, 0.5 mm/year is never exceeded at 130°C. The addition of chlorides in solution has a worsening effect on corrosion rate.

Even in hydrochloric acid (Figure 4-2), corrosion resistance depends on the amount of molybdenum. However, for very dilute solutions, Inconel 625 performs better than other superalloys, even those containing more molybdenum. At room temperature, all superalloys represented, have corrosion rates less than 0.13 mm/year.

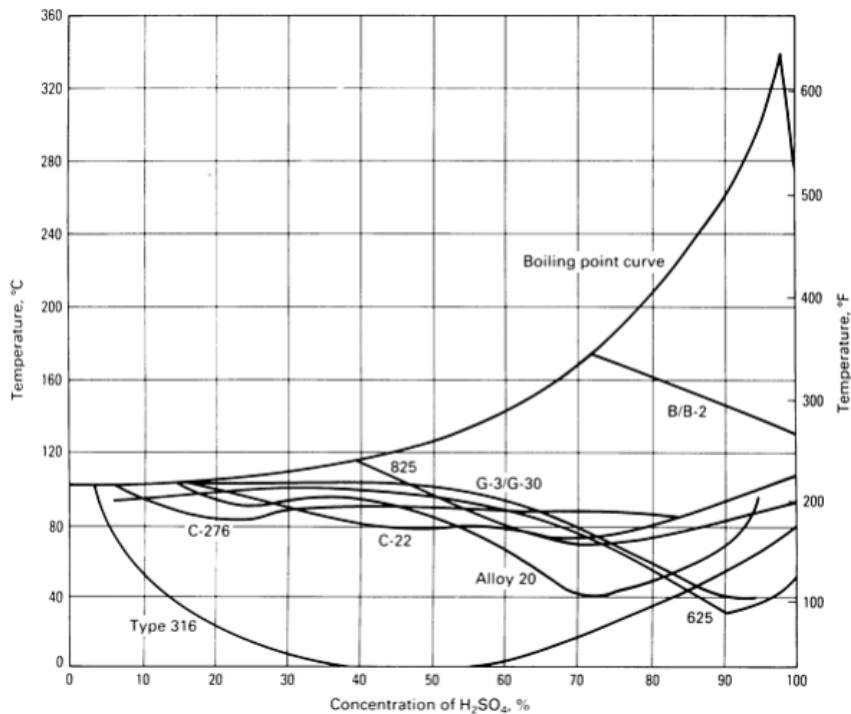


Figure 4-1: Iso-corrosion curves of nickel-based alloy in H_2SO_4 solutions. The lines indicate a corrosion rate of 0.5 mm/year [78].

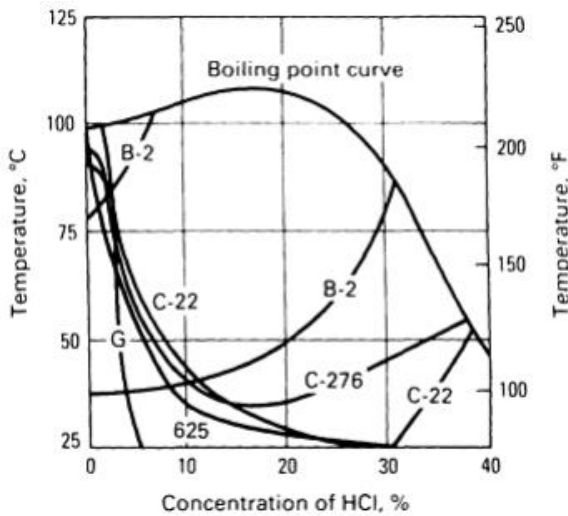


Figure 4-2: Iso-corrosion curves of nickel-based alloys in HCl containing solutions. The lines indicate a corrosion rate of 0.13 mm/year [78].

4.2 Localized corrosion

As is well known, pitting and crevice affect active-passive materials under passivity conditions and depend on environmental factors including chloride concentration, pH, from the cathodic process, and temperature. The presence of anions that stabilize the passivity film, such as chromates, the

presence of interstitials, microstructural inhomogeneities, surface oxides, and roughness also play an important role.

Figure 4-3 shows that the chloride concentration required to initiate pitting drops exponentially for both stainless steels and nickel superalloys. Alloy 625 undergoes pitting for 100 times higher chloride concentrations than AISI 316 at the same pH in the test environment.

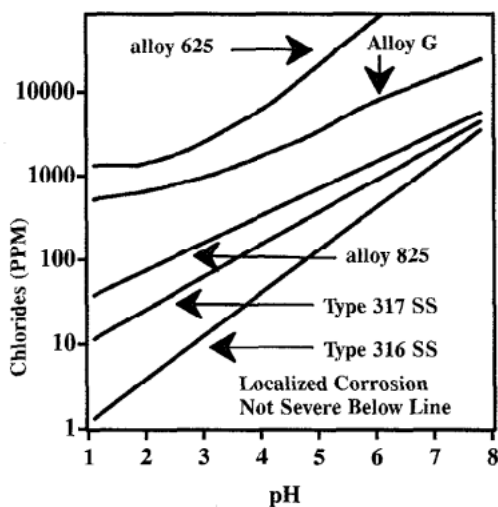


Figure 4-3: Corrosion behavior of different alloys in SO_2 [79].

The empirical index that measures susceptibility of stainless steel and nickel-based alloys to pitting corrosion is called Pitting Resistance Equivalent Number (PREN) [80]. The higher the PREN, the greater the material's resistance to pitting in the presence of chlorides. It is defined as:

$$PREN = wt\%Cr + 3.3(wt\%Mo + 0.5wt\%W) + 16wt\%N$$

Inconel 625 has a high chromium and molybdenum content. These elements promote the formation of passivity films and make it the alloy that is not very susceptible to pitting. Lorenzoni et al [81] provided further confirmation of the link between PREN and pitting manifestation on Inconel 625. From EDS analysis on different portions of the material, they were able to calculate the PREN related to each portion and compare its value with the actual presence of pitting. The importance of the cooling rate also emerged, which affects the

precipitates that nucleate and deplete the matrix of elements that increase the local PREN leading to a localized increase in pitting susceptibility.

In accordance with ASTM G48 [82], there are two empirical indices for estimating the temperature below which pitting or crevice does not occur for nickel superalloys.

These indices, called critical pitting temperature (CPT) and critical crevice temperature (CCT), are defined in the standard:

$$CPT[^\circ C] = 2,5(wt\%Cr) + 7,6(wt\%Mo) + 31,9(wt\%N) - 41,0$$

$$CCT[^\circ C] = 1,5(\%Cr) + 1,9(\%Mo) + 4,9(\%Nb) + 8,6(\%W) - 36,2$$

MCCoy et al [83] indicated a minimum CPT limit of 40 for offshore uses.

Concerning crevice, the mechanism of initiation and propagation in metallic materials in chloride solutions is now well known. In the presence of a very small defect, such that the diffusion of oxygen is hindered, a macro couple is created by differential aeration between the outside and the defect, which leads to an increase in chloride concentration until the passivity film breaks down. Davies-Smith et al [84] studied the effect of niobium alloyed in Inconel 625 on the crevice phenomenon under seawater conditions. Niobium is not only able to strengthen the austenitic matrix by increasing its mechanical properties, but also limits the precipitation of chromium carbides by binding with carbon. Tests have shown that a 2.53 % niobium content in a heat-treated alloy is sufficient to achieve maximum crevice strength by niobium alloying, while 1.66 % is sufficient for an annealed alloy. In the annealed state, therefore, the crevice strength is higher. In fact, niobium also appears in the CCT index.

4.3 Intergranular corrosion

Intergranular corrosion in austenitic matrix materials is due to the precipitation of carbides at the grain boundary that go on to deplete the matrix in neighboring zones of chromium, delineating continuous paths of lower corrosion resistance called sensitized zones. In the wet corrosion

mechanism, the chromium-rich precipitates will act as the cathode, while the sensitized zones, having little chromium, as the anode

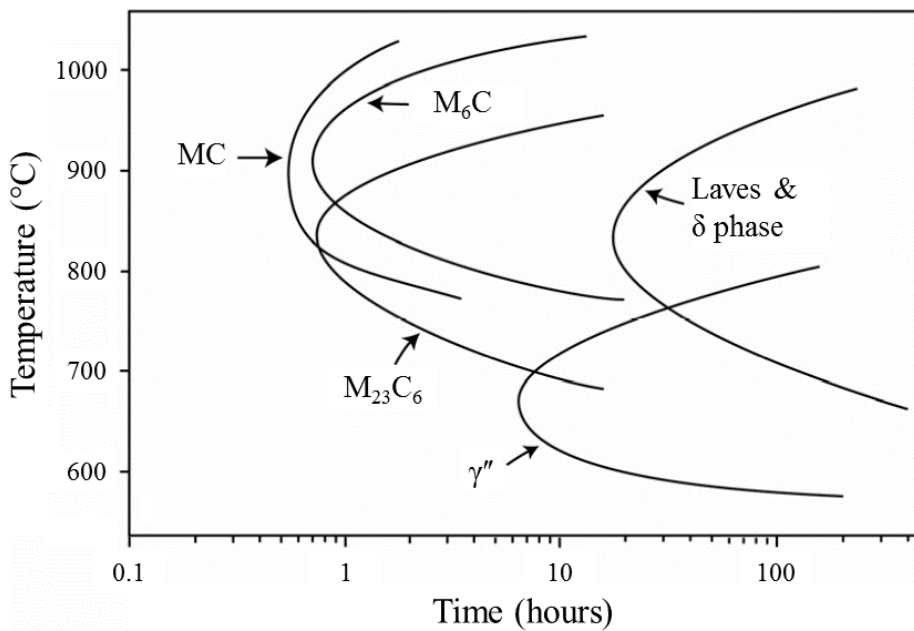


Figure 4-4: TTT diagram of Alloy 625 [85].

Referring to the time temperature transformation (TTT) diagram in Figure 4-4, to avoid sensitization it is necessary to schedule heat treatments and cooling rates in order to avoid the precipitation of $M_{23}C_6$ carbides, in which carbon is known to often alloy with chromium. Rapid cooling is therefore necessary following high-temperature treatments. In alloy 625 and other nickel superalloys, small percentages of niobium, tantalum, and titanium are added to the alloy, which, by precipitating with carbon, reduce its availability by preventing it from bonding with chromium.

Tawancy et al [8] studied the role of niobium precipitates in the corrosion of annealed Inconel 625 and at various stages of aging in boiling 10% nitric acid. What they saw was that niobium precipitates, created as a result of aging, may be the preferential object of selective corrosion, in place of the decromized zones.

4.4 Effect of AM technologies on corrosion behavior

As already noted in previous chapters, components made with AM techniques are characterized by macro and microstructural differences compared to those obtained through traditional processes, which may affect the mechanical and corrosion behavior of materials.

Regarding LPBF and DED processes, the material is subject to a complex thermal cycle that includes rapid local heating above the melting temperature of the material, even faster cooling, and subsequent repeated heating and further cooling as the tracks created by the energy source follow one another. The scanning strategy generates complex microstructures far from those of equilibrium, with phases and arrangement of these very different, difficult to predict.

Marchese et al. [86] reported the presence of Nb- and Mo-rich zones in the interdendritic areas formed upon high cooling rates, developed during solidification in the LPBF process. Instead, Hu et al. [87] identified Laves phases in the DED-LB-produced alloy. The presence of such microstructural features should be carefully assessed, because Laves and other intermetallic phases can significantly enhance the risk of crevice and pitting corrosion in operating conditions, as reported by Guo et al [88]

Cabrini et al [89] highlighted how the role of the microstructure is fundamental in defining the morphology of corrosion forms. The results of the intergranular corrosion tests on hot-rolled and LPBF-processed Alloy 625 specimens showed that the intergranular attack is more evident along the contour of the melt pool. Despite this, the corrosion rate on both untreated and heat treated LPBF specimens was found to be about half that of hot-rolled specimens, denoting a positive effect of AM technology.

The MFFF technology the alloy 625 is barely mentioned in the literature [90,91] and the currently available studies do not perform an in-depth

investigation of the defects, microstructure and, most importantly, corrosion behavior. The determination of the corrosion behavior is fundamental to address, since the alloy 625 alloy is often used in very aggressive environments. Moreover, this material is characterized by greatly differing microstructures, depending on the AM technology adopted for production.

EXPERIMENTAL METHODOLOGY

The purpose of the experimental activity is the characterization of the corrosion behavior of the Alloy 625 obtained by means of LPBF, DED and MFFF technologies and its comparison with the same alloy obtained by means of traditional technique. As a reference material, a bar obtained by hot rolling, in the metallurgical state of grade 1, intended for use in the oil and gas field, was chosen.

MFFF and DED specimens were manufactured at the ENEA Research Centre of Casaccia (Rome), while the LPBF samples had already been made at the Politecnico di Torino for a previous experimentation.

The corrosion behavior assessment was carried out at the University of Bergamo by means of potentiodynamic and potentiostatic polarization tests and susceptibility to intergranular corrosion tests. Metallographic analysis was also carried out to identify the effect of different AM techniques on mechanical properties and corrosion behavior.

The effect of post-processing treatment was evaluated for AM specimens.

5.1 Feedstock materials

A gas atomized powder, supplied by EOS GmbH, was used for LPBF specimens. The distribution of the powders size is within the range with a d_{10}

Chapter 5

Experimental methodology

of 16 μm , d_{50} of 27 μm and d_{90} of 48 μm . The composition of a printed part reported in Table 5-1 was evaluated via inductively coupled plasma (ICP) and LECO analysis by Politecnico di Torino [71].

The MFFF-manufactured specimens were built by using Markforged Inconel 625, a commercial metal powder-polymer filament characterized by a diameter of approximately 1.8mm. This filament is guaranteed to meet chemical requirements of ASTM B443 standard [13], after printing, washing, and sintering processes [92]. The composition of a printed was evaluated via inductively coupled plasma (ICP) and LECO analysis to determine the main alloying elements and C content, respectively (Table 5-1).

The DED-built specimens were realized using a 1.2 mm diameter commercial welding wire NICROFER S6020 FM625 by VDM Metals. The heat analysis of the wire is reported in Table 5-1.

Table 5-1: Composition of the feedstock materials used.

Element [wt%]	LPBF part	MFFF part	DED wire *	HW *
Ni	Bal	Bal	Bal	Bal
Cr	22.4	19.55	22.31	21.6
Mo	8.2	8.57	9.03	8.26
Nb	3.73	3.28	3.47	3.66
C	0.01	0.08	0.01	0.036
Co	0.17	0.047	0.01	0.02
Al	<0.01	<0.001	0.10	0.199
Ti	0.18	0.022	0.22	0.243
Fe	0.45	2.61	0.19	3.11
Si	0.08	0.52	0.07	0.25
Mn	0.03	0.40	0.01	0.19
Ta	0.13	-	0.01	0.01
P	<0.001	0.006	0.003	0.007
S	0.002	0.004	<0.001	0.001
N	-	-	0.023	-
Cu	-	-	<0.01	-

*Heat analysis

For comparison purpose, a 16 mm diameter hot worked (HW) bar was considered. The bar was supplied in the grade 1 state (according to ASTM B446 [93]), after annealing at 980°C for 32 min, followed by water quenching. The chemical compositions of the feedstock materials are reported in Table 5-1.

5.2 Specimens

The LPBF specimens were manufactured by using an EOSINT M270 Dual Mode machine, operating in an argon atmosphere. The process parameters and scanning strategy were optimized in order to produce parts with very low porosity, as reported in published work [52]. Cubic specimens of 15 mm side and disks of 15 mm diameter and 5 mm height have been fabricated.

MFFF specimens were obtained by using a Metal X Markforged System. The manufacturing operation consisted of three main steps: printing a green part of metal powder bound in a polymer matrix, debinding and then sintering. The only process parameter that can be chosen throughout the process is scanning strategy. The single layer scan strategy involved the deposition of 4 stripes of contour on the external sides (named wall layers) and the deploying of the inner part with a $\pm 45^\circ$ scanning strategy (named infill). Between two successive layers, the stripes deployed in the inner part change orientation, while the contour was characterized by parallel stripes maintaining the same orientation. Figure 5-1 shows a schematic illustration of the scanning strategy adopted.

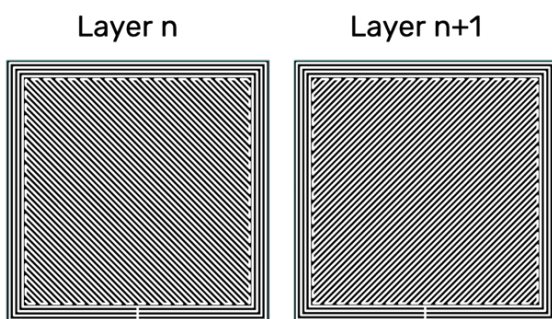


Figure 5-1: Schematic representation of the scanning strategy adopted for the MFFF-manufactured specimens.

After printing, chemical debinding for removing the binder was carried out by immersing the green part in a boiling Opteon SF79 solvent (60-100% of trans-1,2-dichloroethylene, 1-5% of fluorocarbon and <1% of 1,1,2,2,3,4,5,5,5-decafluoropentane) in a Markforged Wash-1. The duration of the debinding phase has been suggested by the printing software and depends on the material and geometry of the component. To verify a correct debinding, the specimens were weighed before and after the process to meet the mass change constraints indicated by the manufacturer. The final sintering phase was carried out in a Markforged Sinter-1 furnace, operating in a protective argon gas flow for about 27 hours. The temperature and gas flow adopted are preset parameters and not disclosed by the manufacturer. 15x15x15 mm³ cubic specimens and 15 mm diameter and 5 mm height disk have been fabricated.

DED samples were built by means of a custom-made system in ENEA laboratory. The apparatus was equipped with a YLS-4000 from IPG Photonics, a 4 kW Yb laser, characterized by a 1060 nm wavelength and a fixed focal length of 250 mm. During the process, the laser beam has been defocused to increase beam diameter. An external wire feeding system provides material feedstock in the melt zone at an angle of 30° to the deposition plane. Finally, an external nozzle close to the deposition area provided an argon flow rate of 10 liters per minute to prevent oxidation.

In the first part of the experimentation, different combinations of process parameters, modifying laser power, wire feeding rate, defocusing distance were employed. Moreover, for some of these combinations a circular oscillation of the laser beam of 0.5 mm diameter at 200 Hz was used (laser wobbling). For the process parameter optimization, a raster deposition scan strategy was employed to build 30 mm length thin wall specimens using a hatching distance of 1 mm between the two contiguous stripes deposited on a stainless steel AISI 316 substrate. The different set of process parameters from D1 to D15 are reported in Table 5-2.

For all the process parameter combination, a 17 mm/s constant speed of the deposition head was used.

Table 5-2: Different process parameters used for DED-manufactured samples.

Sample	Laser power [W]	Wire feed rate [m/min]	Defocusing distance [mm]	wobbling
D1	1500	1.04	25	No
D2	1800	1.04	25	No
D3	1800	1.04	25	Yes
D4	1500	1.3	25	No
D5	1500	1.3	25	Yes
D6	1800	1.3	25	No
D7	1800	1.3	25	Yes
D8	1500	1.04	20	No
D9	1500	1.04	20	Yes
D10	1800	1.04	20	No
D11	1800	1.04	20	Yes
D12	1500	1.3	20	No
D13	1500	1.3	20	Yes
D14	1800	1.3	20	No
D15	1800	1.3	20	Yes

All these specimens were sectioned along the building direction and macro- and microstructural analyses and hardness tests were carried out in order to select a set of parameters with which realize the samples for the characterization of corrosion behavior.

Based on the results obtained, the combination of parameters D15 was chosen for the realization of the specimens for subsequent experimentation. Thin-walled specimens of approximately 240 mm length and 110 mm height were fabricated by the deposition of 3 stripes of feedstock material with a hatching distance of 1.5 mm, using a raster scan strategy (Figure 5-2). For

microstructural analysis and corrosion tests disk samples of 15 mm diameter and 5 mm height and 25·25·3 mm³ samples were extracted by the thin walls by means of electro discharge machining (EDM) using a HB600 SSG wire cutting machine, equipped with a 0.018 mm Mo wire. The area from which the samples were extracted was chosen in order to avoid any alteration in the chemical composition of the material due to the dilution process between the substrate made of AISI 316 stainless steel and Inconel 625

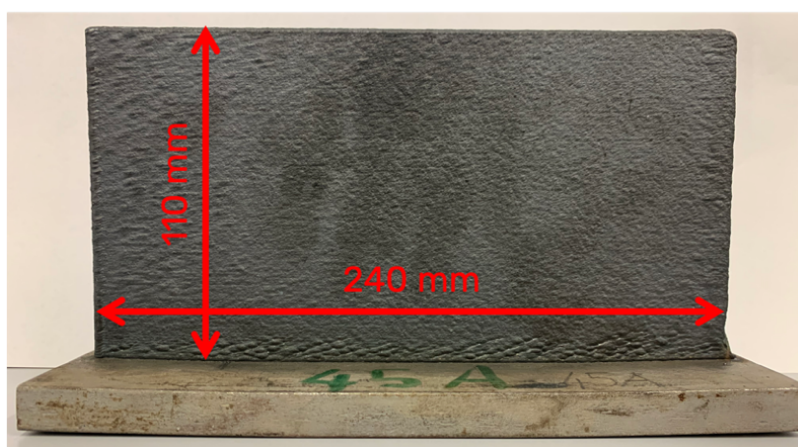


Figure 5-2:DED-manufactured thin wall.

Finally, 5 mm-tall disk specimens were obtained from the hot worked bar by means of mechanical cutting.

5.3 Post process heat treatment

Tests have been carried out on as-produced untreated specimens (named UT) and after post-process heat treatment. Specifically, the LPBF specimens were heat-treated at the Politecnico di Torino by performing an annealing at 980 °C for 32 minutes in a muffle furnace followed by water quenching (LPBF HT). The MFFF and DED samples underwent a hot isostatic pressing process (named MFFF HIP and DED HIP respectively) by a QIH 21 – 2070 – 1450M URC & 1400M URQ hot isostatic press system by Quintus. The specimens were hipped at 1150°C for 3 hours at 160 MPa in an inert argon atmosphere. Temperature and pressure trends versus time are shown in the Figure 5-3. At the end of the cycle, the available rapid cooling mode was used to return temperature and pressure to the initial value.

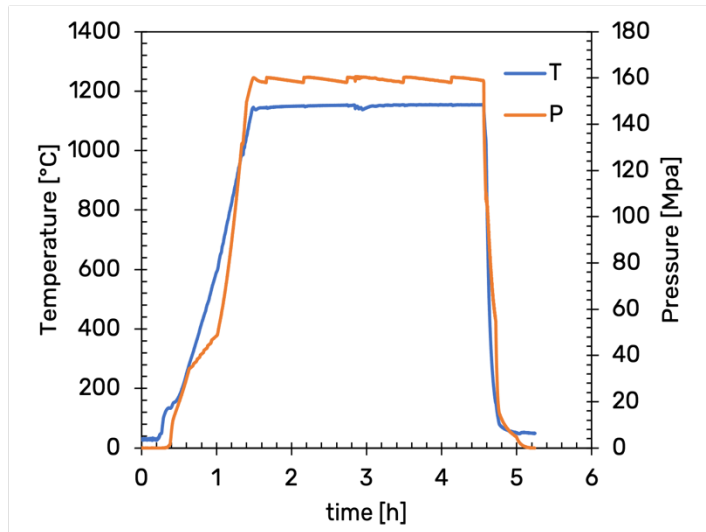


Figure 5-3: Temperature and pressure versus time during the HIP process performed.

5.4 Metallographic analysis

The metallographic analysis was performed on the cross section obtained by cutting the AM-produced specimens along the building direction. For the HW specimen, the analysis was performed on the cross section perpendicular to the rolling direction.

All the specimens were firstly ground using silicon carbide emery papers and subsequently polished up to 1 µm diamond paste.

Porosity evaluation of the cross sections were performed by means of a Keyence VHX-7100 digital optical microscope through digital image analysis by ImageJ software.

Microstructure characterization was performed by the observation of metallographic cross section after chemical etching with Kalling n.2 reagent (5 g CuCl₂, 100 ml HCl, 100 ml CH₃CH₂OH). The analysis was then deepened by observation carried out using a Zeiss EVO 50 scanning electron microscope (SEM), equipped with an Oxford X-Act probe for energy dispersive X-ray spectroscopy (EDS)

5.5 Intergranular corrosion tests

The susceptibility to intergranular corrosion tests were carried out on the cubic samples for MFFF technology, while the DED plates were made into 25x25x3mm test pieces. The results obtained by Testa on the LPBF and HW specimens were used for comparison [71]. The 120-h test in boiling ferric sulphate/sulphuric acid solution was carried out in compliance with ASTM G28, method A [94].

Prior to the test, the surfaces of the specimens were polished with silicon carbide emery papers up to 1200 gritt. Moreover, two sides were polished up to the 1 µm diamond paste to allow observation of the corrosion morphology. Just before immersion in the test solution, the specimens were rinsed with distilled water, cleaned in acetone by ultrasonic bath and dried. Before and after the test, the specimens were weighed with an analytical balance to assess weight loss.

The corrosion rate was evaluated in terms of mdd (milligrams per square decimeter per day) by the equation 4-1:

$$V_{corr} = \frac{W}{A \cdot T} \quad \text{Eq. 4-1}$$

where:

- W in the mass loss of the sample in mg
- A is the exposed surface in dm^2
- T is the exposure time in day

After the test, the surfaces were then observed by means of scanning electron microscope to observe the corrosion morphology.

Finally, metallographic cross sections were obtained for was observing the morphology of the attack penetration.

5.6 Potentiodynamic polarization tests

Potentiodynamic polarization tests were performed on disk specimens by using a Gamry Reference 600 potentiostat. The testing surfaces were firstly ground using SiC emery papers and subsequently polished up to 1 µm diamond paste. Before the tests, all the specimens were ultrasonically cleaned in acetone at room temperature, dried and allowed to passivate for 1 hour.

The tests were performed in a 1-liter standard three electrode cell (ASTM G5 [95]) equipped with a PTFE sample holder having a circular exposed area of 10 mm diameter, a Saturated Calomel Electrode (SCE) placed in a Huber-Luggin capillary probe, and two graphite counter electrodes.

The testing solution was de-oxygenated by means of nitrogen gas purging maintained throughout the whole test duration. A thermostatic water bath provided constant temperatures. The potentiodynamic tests were conducted in three testing solutions:

- 1 N H₂SO₄ solution – according to ASTM G5 [95] at 30°C
- Neutral chloride solution (0.6 M NaCl, pH 7) at 40°C
- Acidified chloride solution (0.6 M NaCl + HCl, pH 3) at 40°C

Before the tests, the open circuit potential (OCP or E_{corr}) was monitored until stability was achieved. The potentiodynamic polarization tests in 1N H₂SO₄ solution were carried out according to ASTM G5 standard [95] using a 10 mV/min scan rate from E_{corr} value up to 1.6 V vs SCE. Using the same scan rate, for the cyclic potentiodynamic polarization tests in chloride solutions the polarizations were conducted from 10 mV below the OCP value up to 1 V vs. SCE or until the anodic current density reached 10 mA/cm². Afterwards, a reverse scan returned the potential to the initial OCP value.

After the tests, the specimens were firstly washed with distilled water, rinsed with acetone in ultrasonic bath, and finally dried. Corrosion morphologies were observed by means of optical and scanning electron microscope.

5.7 Potentiostatic polarization tests

Potentiostatic polarization tests were carried out in both the chloride solutions at +200 mV and +500 mV vs. SCE for 24 hours, with an acquisition rate of 1 Hz. The setup was the same used for potentiodynamic polarization tests. Before the test, the OCP was monitored for 1 hour.

After the tests, the specimens were washed with distilled water, rinsed with acetone in ultrasonic bath, dried and finally were observed by SEM in order to observe corrosion morphologies.

5.8 Hardness tests

Low force Vickers hardness was measured according to UNI EN ISO 6507-1 by means of a UHL VMHT microhardness equipment applying a load of 1000 gf for 15 s. The tests were performed on the polished cross sections up to 1200 gritt and were repeated to assess hardness variation along the building direction.

RESULTS

6.1 DED process parameters optimization

Figure 6-1 shows some of the specimens realized for the process parameters optimization for DED technology.



Figure 6-1: Morphological appearance of some of the specimens made for the optimization of DED process parameters. a) D15, b) D11 and c) D5.

From the point of view of morphological appearance, some thin-walled specimens show a stable deposit (specimen D15 in Figure 6-1a). Conversely, a progressive reduction in height along the direction of deposition was observed with some combinations of process parameters (specimen D11 in Figure 6-1b). Moreover, as in the case of specimen D5 shown in Figure 6-1c, some specimens are characterized by macro defects that drastically reduce the cross section of the deposit.

To compare the different set of process parameters, the evaluation of the maximum and minimum thin-walled thicknesses on the cross sections was also carried out by means of an optical profile meter. The results shown in

Chapter 6

Results

Table 6-1 reveal that although the specimens were made with the same hatching distance between the two scan tracks, the thickness of the deposited thin walls have different values. Specimens D3, D4, D9 and D15 were characterized by the smallest difference between the maximum and minimum thicknesses. Moreover, it was also observed that specimens D5 and D10 have a difference in thickness greater than 1.6 mm, indicative of an unstable deposit along the building direction.

Table 6-1: Cross-section thickness of process parameter optimization specimens D1 to D15.

Specimen	Maximum thickness [mm]	Minimum thickness [mm]	Difference [mm]
D1	3.33	2.76	0.58
D2	3.87	3.12	0.75
D3	3.90	3.44	0.46
D4	3.45	2.99	0.46
D5	3.59	1.92	1.66
D6	4.07	3.18	0.89
D7	4.03	3.46	0.56
D8	3.88	2.92	0.96
D9	3.02	2.59	0.43
D10	4.01	2.39	1.62
D11	3.31	2.27	0.84
D12	3.86	2.78	1.08
D13	3.31	2.27	1.04
D14	3.70	3.03	0.67
D15	3.84	3.41	0.43

The analysis was deepened by the observation of the cross section by optical microscopy. Some examples of micrographs shown in Figure 6-2 highlight that certain combinations of process parameters led to defects such as macro porosity (Figure 6-2a) and cracks at the conjunction between the two scan tracks (Figure 6-2b).

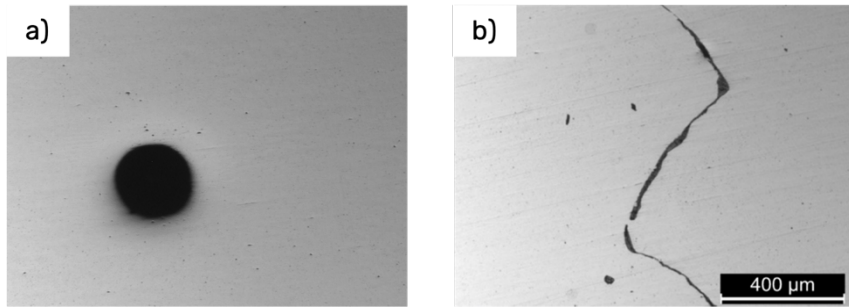


Figure 6-2: Example of defects observed on the micrographs of the cross section. a) macro pore on D8 specimen, b) crack on D1 specimen.

Evaluation of mechanical properties was carried out by low-force Vickers hardness tests performed on the cross-section along the building direction. The results in the Figure 6-3 show that the average hardness values measured along the building direction are uniform for all combinations of process parameters used, ranging from 236 to 251 HV1. Calculated hardness values are similar to those reported in the literature for DED technology [96,97].

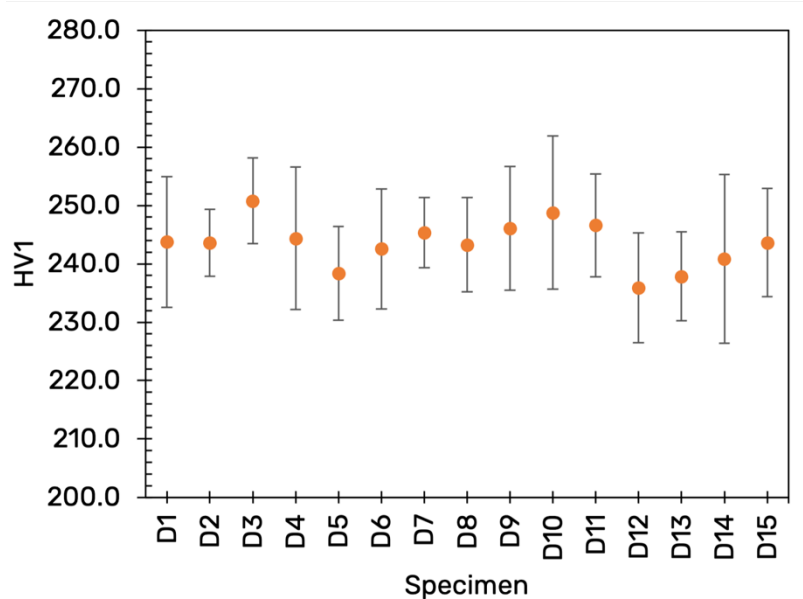


Figure 6-3: Mean value and standard deviation of Vickers hardness of process parameter optimization specimens D1 to D15.

Finally, the feedstock material deposition rate was calculated by the following equation:

$$\text{Deposition rate} = S_{\text{wire}} V_{\text{wire}} \quad \left[\frac{\text{cm}^3}{\text{h}} \right] \quad \text{Eq. 4-1}$$

Chapter 6

Results

Where S_{wire} is the cross section of the wire and V_{wire} is the wire feed rate.

To sum up, the choice of the set of process parameters for making specimens for subsequent experimentation was based on obtaining specimens with:

- geometric stability along the direction of deposition
- least variation in cross-sectional thickness
- absence of macro defects
- higher deposition rate

Table 6-2: Characteristics of the process parameters optimization.

Specimen	Thickness variation [mm]	Geometrical stability	Macro defects	Hardness [HV1]	Deposition rate [cm ³ /h]
D1	0.58	Yes	Yes	244	70.57
D2	0.75	No	Yes	244	70.57
D3	0.46	No	No	251	70.57
D4	0.46	Yes	Yes	244	88.22
D5	1.66	No	No	238	88.22
D6	0.89	Yes	No	243	88.22
D7	0.56	No	No	245	88.22
D8	0.96	No	Yes	243	70.57
D9	0.43	Yes	No	246	70.57
D10	1.62	No	No	249	70.57
D11	0.84	No	No	247	70.57
D12	1.08	No	Yes	236	88.22
D13	1.04	Yes	No	238	88.22
D14	0.67	Yes	No	241	88.22
D15	0.43	Yes	No	244	88.22

From the results shown in the Table 6-2, it was observed that the parameter combination D15 is the one that meets all the selection criteria.

6.2 Porosity analysis

The average porosity of AM specimens under untreated conditions evaluated by means of digital image analysis is reported in Table 6-3. The LPBF- and

DED-processed specimens were characterized by significantly low values. These results tie well with findings in the recent literature [98–100] and confirm that LPBF and DED technologies are currently well established and the relative process parameters are optimized. Conversely, the specimens produced by MFFF process were characterized by significantly higher porosity values.

Table 6-3: Porosity and relative fraction of pores > 50 µm.

AM technology	MFFF	DED	LPBF
Porosity (%)	2.10	0.06	0.06
Pores > 50 µm (%)	0.48	0.02	0

It is well known that an excessive concentration of pores can result in a degradation of the corrosion behavior and mechanical properties [101,102]. It was reported that pores exceeding a 50 µm dimension might be detrimental for the corrosion behavior of AM-processed metals [102]. Therefore, the fraction of pores characterized by a Feret diameter (d_{Feret}) of 50 µm or higher was estimated. No defects above this threshold were found in the LPBF-fabricated specimens. Instead, in the DED- and MFFF-manufactured materials a relevant fraction of pores >50 µm were found, accounting for a total of 33% and 23% of the total porosity, respectively.

The higher overall porosity found in the MFFF-processed material was worthy of a deeper evaluation. The observation of the cross-section of a cubic sample (Figure 6-4) evidenced the presence of two main types of voids:

- Micro-pores, randomly distributed throughout the whole cross section of the specimen
- Elongated macro-pores, having a triangular cross-section shape in the core, quadrilateral in the contour, that are periodically distributed in a grid-like fashion

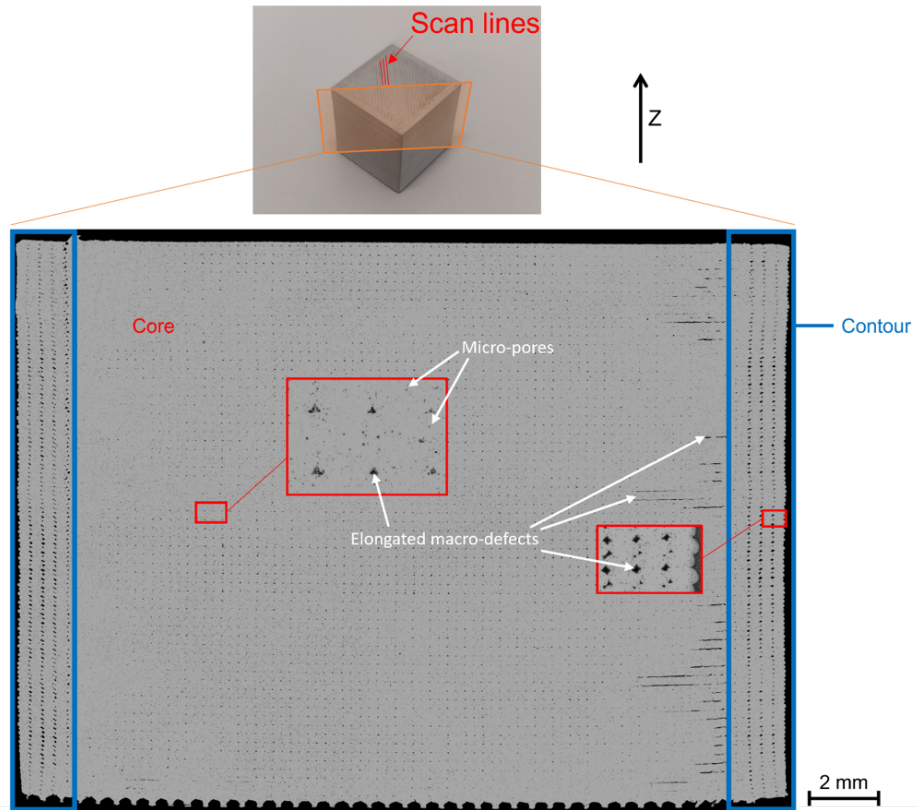


Figure 6-4: metallographic cross-section (45 ° cut) of a MFFF-produced sample with different types of defects highlighted.

The micro-pores were the smallest defects found in the cross-section analysis. The macro-defects were characterized by a periodical arrangement both along the Z axis and horizontally, along deposition plane. Considering a cross-section perpendicular to the deposition lines shown in Figure 6-4, the average distance between two horizontal neighbor macro-defects was quite constant and close to 250 µm. This value corresponds to the width of a post-sintered stripe.

6.3 Microstructural analysis

The optical micrographs obtained from the LPBF-processed samples in untreated condition (Figure 6-5a) highlighted the presence of columnar grains, grown epitaxially along the building direction, and visible melt pools, in agreement with the literature [103]. Instead, the DED UT-processed material was characterized by large dendritic regions (Figure 6-5b), as confirmed by other works [104,105]. Conversely, the MFFF UT-processed

samples (Figure 6-5c) had a precipitates-rich microstructure in a Ni matrix. Moreover, some inclusions were seldom detected inside some pores and accounted for 0.33% of the total cross-section area. The reference HW material (Figure 6-5d) was characterized by equiaxed Ni grains with characteristic twins, a typical outcome for the annealed alloy 625 [106].

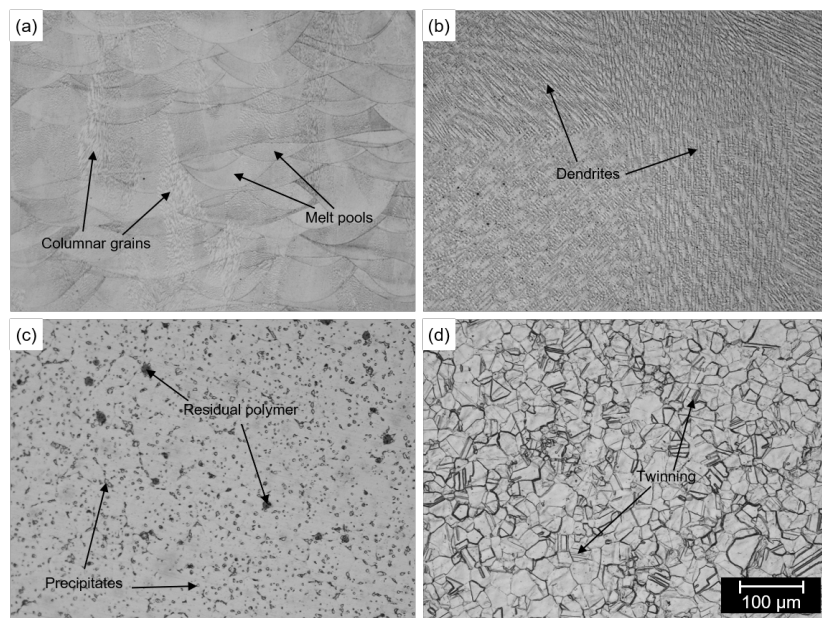


Figure 6-5: Optical microscopy images of the microstructure of the a) LPBF-, b) DED-, c) MFFF-manufactured in untreated condition and d) HW specimens.

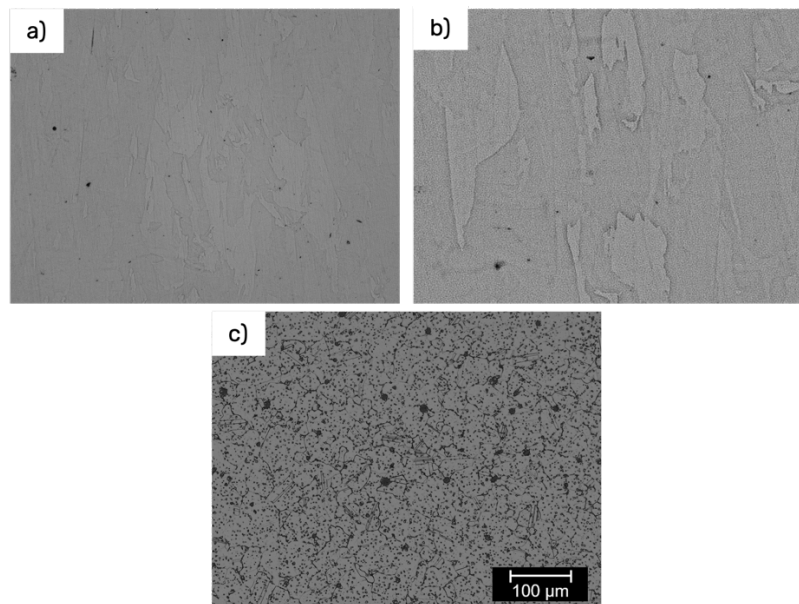


Figure 6-6: Optical microscopy images of the microstructure of the a) LPBF HT, b) DED HIP and c) MFFF-HIP specimens.

Chapter 6

Results

Post-process heat treatments change the microstructure of the material. In fact, in LPBF specimens subjected to grade 1 heat treatment, melt pools are no longer visible and columnar grains which are aligned along the building direction were observed (Figure 6-6a) as confirmed by Testa [71]. DED HIP specimens are also characterized by columnar grains aligned with the building direction, which are larger in size than those of LPBF HT (Figure 6-6b). MFFF HIP specimens, on the other hand, retain the equiaxial austenitic structure, but a reduction in grain size was observed compared with untreated conditions (Figure 6-6c).

A further microstructural characterization was conducted via SEM imaging on the untreated specimens (Figure 6-7). The LPBF-processed samples (Figure 6-7a) provided a dendritic/cellular microstructure. Nb and Mo segregations were detected in correspondence of the interdendritic regions, in agreement with other works in the literature [107,108]. Moreover, no precipitates were found. However, Marchese et al. [109] demonstrated via transmission electron microscopy analysis (TEM) that very small (<100 nm) Nb-rich MC carbides are present in the LPBF-manufactured material.

Conversely, Mo-rich precipitates were detected in the interdendritic regions of the DED-processed specimens (Figure 6-7b), as confirmed by Abioye et al. [110]. These were identified as Laves phases by Yangfan et al. [111]. Moreover, some small ($\approx 1 \mu\text{m}$) oxide inclusions were also found. Similarly, spherical oxides rich in Ti, Al and Cr were also detected by Huebner et al. [112]. These were probably generated during the manufacturing operations due to the high affinity of these elements with oxygen and the lack of a sealed process chamber [113,114].

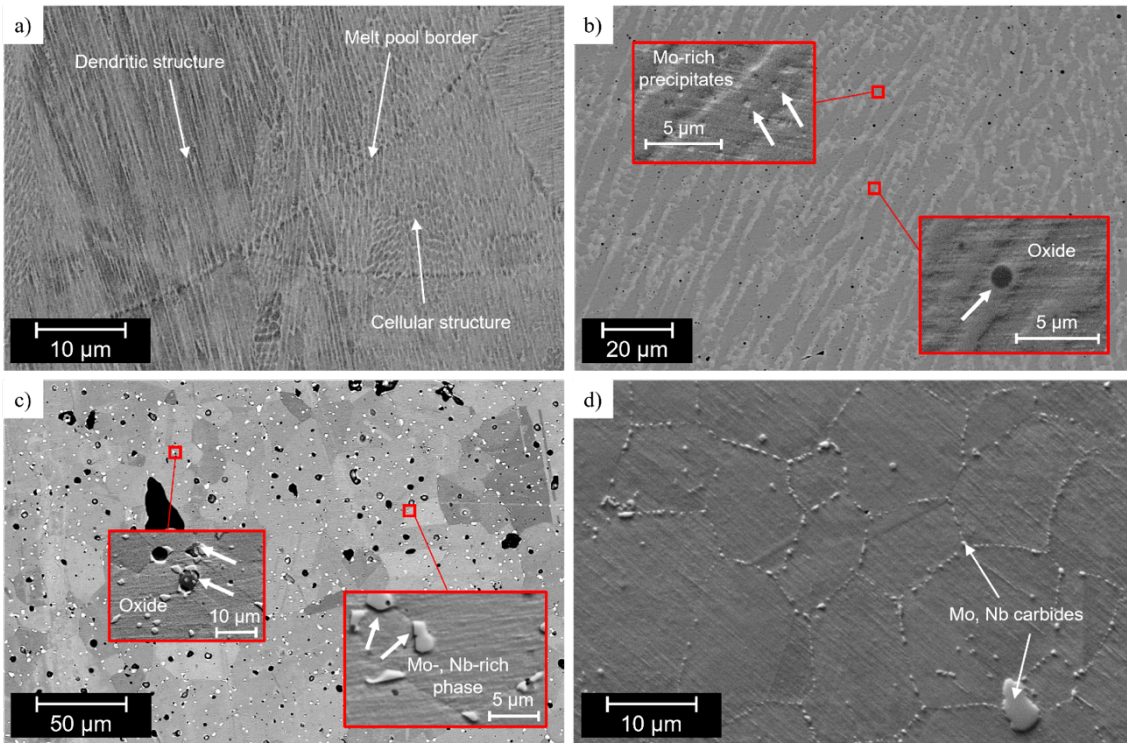


Figure 6-7: SEM images of the microstructure of the a) LPBF-, b) DED-, c) MFFF-manufactured and d) HW specimens.

In the MFFF-processed specimens, similar oxide inclusions (Figure 6-7c) were also detected. These were found to be rich in Al, Si and Cr by EDS analyses (Figure 6-8). It is worth noticing that these oxides were surrounded by secondary phase. The formation of oxidized areas, alongside carbides, is expected to form during the debinding/sintering phases as a result of impurities pick-up [115]. Working on the MFFF-processed Inconel 718 alloy, similar considerations were also made by Thompson et al. [116]. Carbides were found throughout the whole microstructure of the MFFF-processed material in a blocky shape both inside and at the border of grain boundaries. SEM observations also evidenced the presence of a second phase (Figure 6-7c), evenly dispersed in the material (approximately 3.2% in volume). It was abundantly found in correspondence of grain boundaries and pore/inclusion edges, more seldom inside the grains. This secondary phase was rich in Mo, Nb and Si (Figure 6-9a). By comparing its EDS spectrum with the one relative to the matrix (Figure 6-9b), a slight enrichment in C was also detected in this second phase. Moreover, it appeared depleted in Ni, Cr and Fe with respect

Chapter 6

Results

to the matrix. The reference HW material was characterized by elongated carbides, forming semi-continuous chains along the γ grain boundaries, in agreement with the literature [117]. The second phase was constituted of MC-type carbides, rich in Mo and Nb, whose elongated shape is due to the low cooling rate achieved at the end of the hot working process [118].

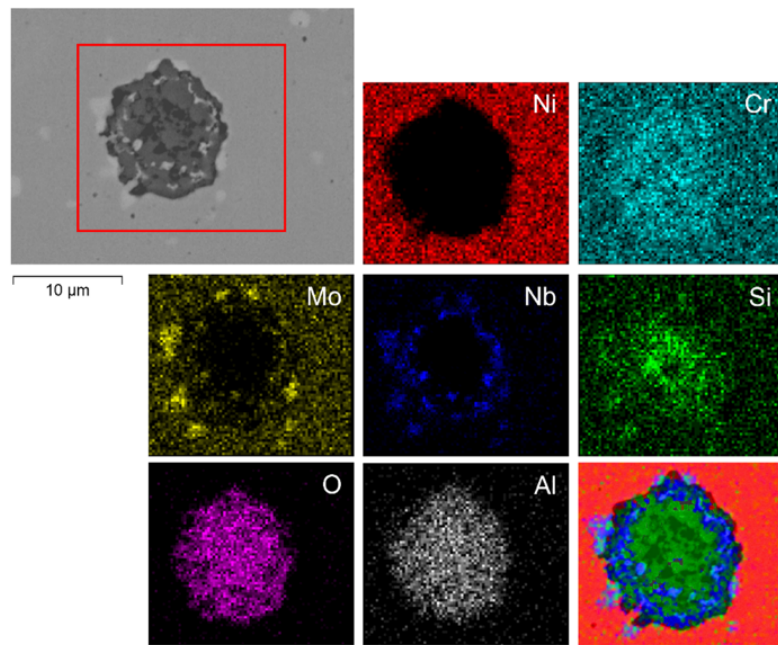


Figure 6-8: EDS map analysis covering an oxide inclusion found in the MFFF-manufactured alloy 625.

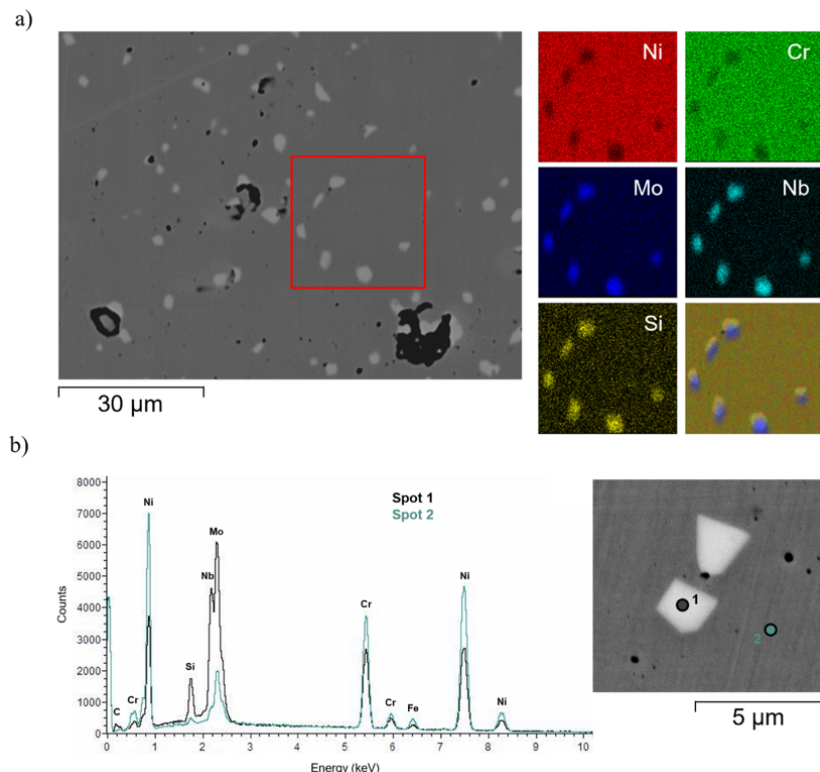


Figure 6-9: EDS map a) performed on MFFF-processed specimen and b) relative comparison of the diffraction pattern of the secondary phases found and the matrix.

6.4 Intergranular corrosion tests

Susceptibility to intergranular corrosion tests were conducted to evaluate the corrosion rates of the alloy 625 processed using different AM technologies. The results, presented in Table 6-4, were also compared with the HW reference material.

Table 6-4: Corrosion rates evaluated according to ASTM G28 method A [94]. The data relative to the LPBF-produced and HW specimens come from a previous publication [89].

Specimen	Exposed surface (cm ²)	Mass loss (g)	v_{corr} (mdd)	Source
LPBF UT	13.4	0.112	167	[89]
LPBF HT	13.1	0.073	112	[89]
MFFF UT	15.2	0.163	214	-
MFFF HIP	11.3	0.116	206	-
DED UT	12.8	0.069	108	-
DED HIP	15.2	0.074	98	-
HW	6.1	0.105	346	[89]

The DED-processed material provided an excellent corrosion rate, whilst the MFFF-manufactured specimens provided the highest v_{corr} among all the AM technologies considered. Notwithstanding that, this value was significantly lower than the HW. The significantly higher corrosion rate of this latter condition was mainly due to grain dropping phenomena occurring during the test, as already discussed in a previous work [89].

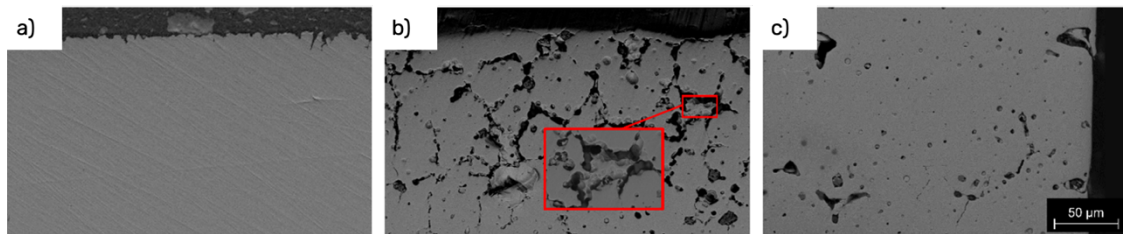
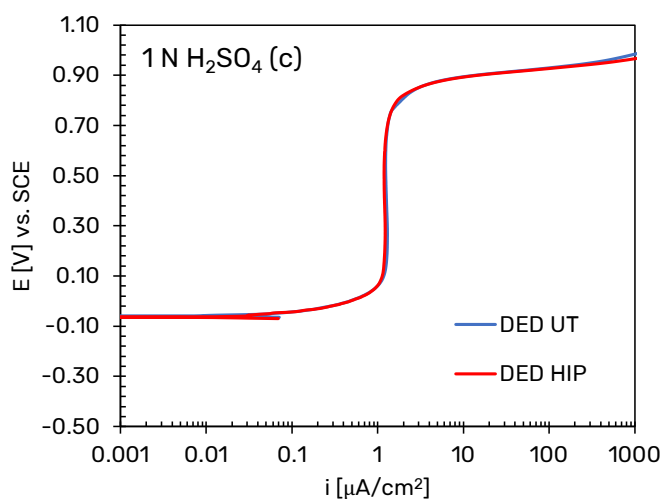
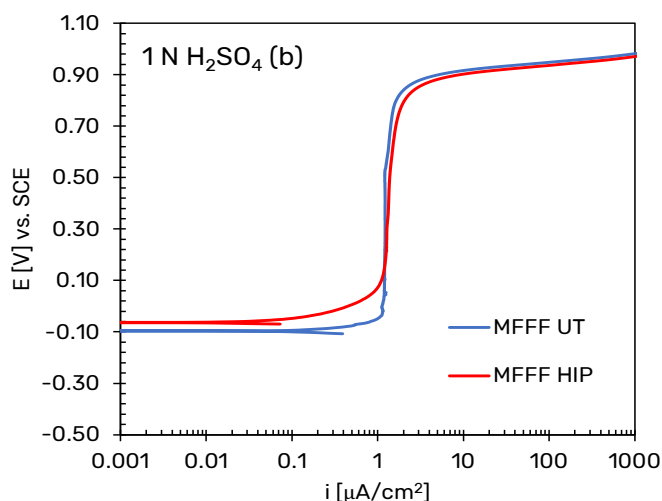
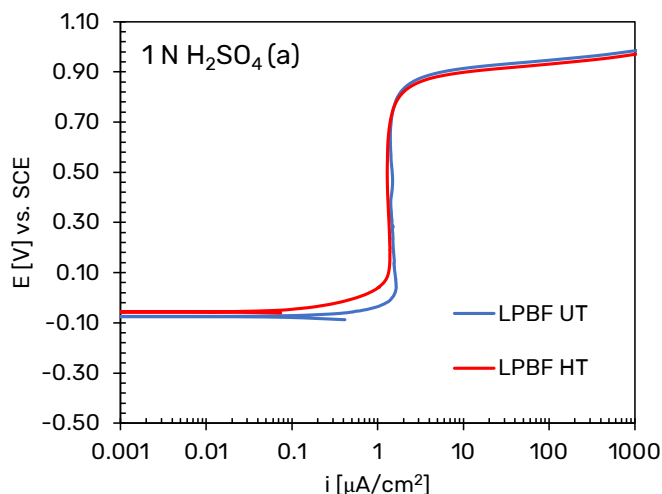


Figure 6-10: Different response during the susceptibility to intergranular corrosion test. a) DED UT-processed specimen b) core region of the MFFF UT-processed material c) contour region of the MFFF-processed material.

No significant proofs of an intergranular attack were found in the LPBF and DED-processed material (Figure 6-10a). Conversely, the MFFF-manufactured specimens provided a dissimilar behavior during the test, according to the area of the sample considered. This phenomenon is illustrated in Figure 6-10b,c. The core portion of the material highlighted a penetrating attack, following the grain boundaries and macro-defects, extending for more than 200 μm (Figure 6-10b). Oppositely, the contour provided only a limited number of isolated attacks (Figure 6-10c).

6.5 Potentiodynamic polarization tests

The results of potentiodynamic polarization tests in H_2SO_4 1N solution (ASTM G5 [95]) are shown in Figure 6-11.



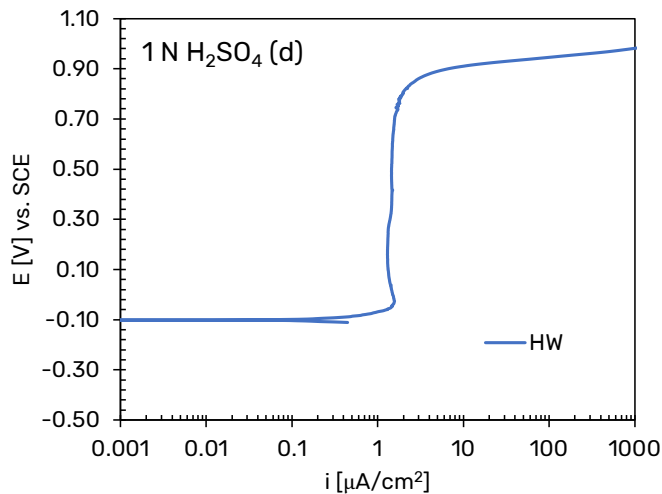
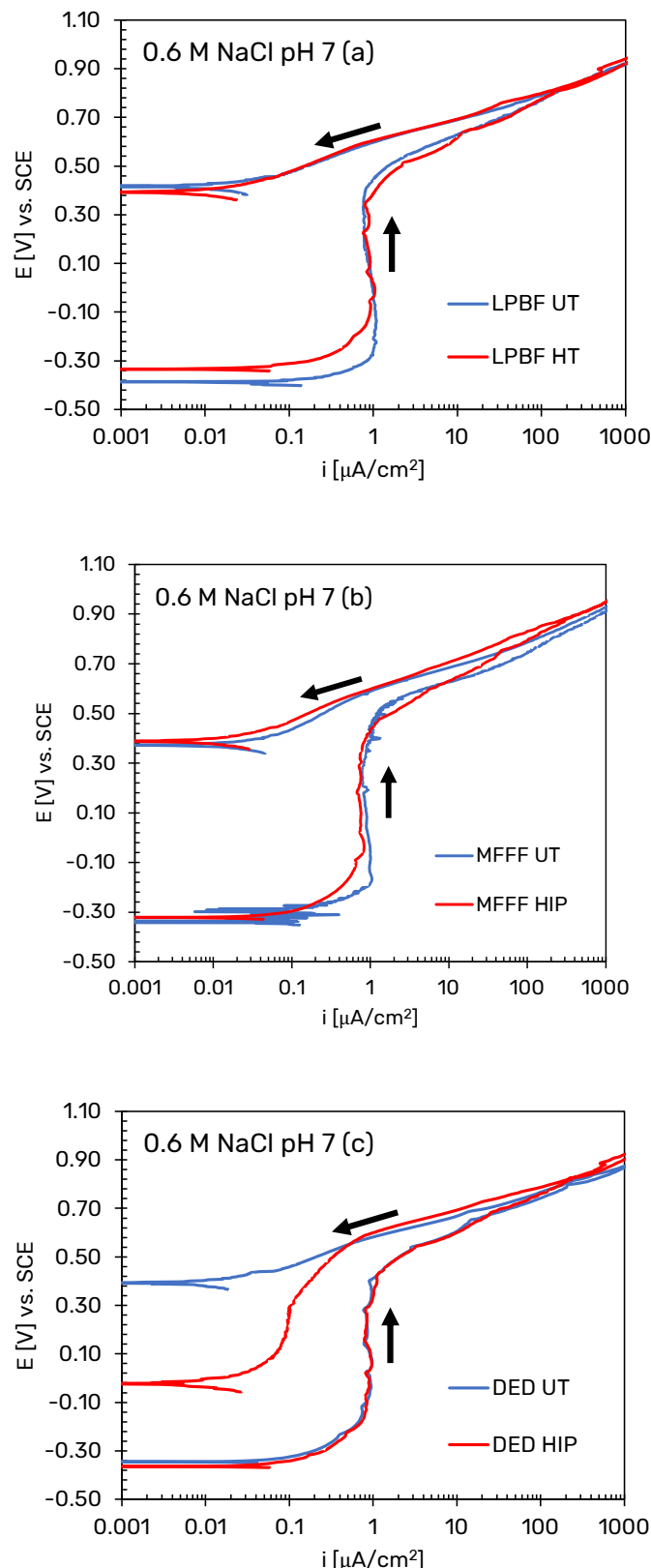


Figure 6-11: Potentiodynamic polarization curves in 1N H_2SO_4 solution: a) LPBF-, b) MFFF-, c) DED-manufactured samples and d) HW sample.

After immersion in the test solution, it was observed that the value of free corrosion potential E_{corr} takes slightly different values among different technologies, with a general tendency of a nobler potential for specimens obtained by means of AM technologies compared to the HW condition (Figure 6-11d). Particularly, for LPBF and MFFF technology, E_{corr} is greater for post-processed specimens than for untreated conditions (Figure 6-11a and Figure 6-11b), whereas in DED technology, no differences were observed between untreated and hipped conditions (Figure 6-11c).

All the curves showed a passive behavior over a wide range of potentials up to an increase in the anodic current density for potential values corresponding to the development of oxygen. No differences were found in the value of the anodic current density i_p in the passive range, which takes a value of about $1 \mu\text{A}/\text{cm}^2$. This behavior indicates that in this environment the alloy does not undergo corrosion, in agreement with the literature [119].



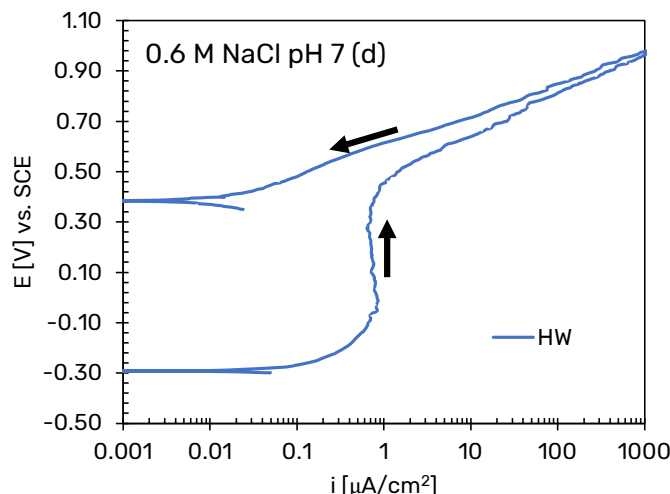
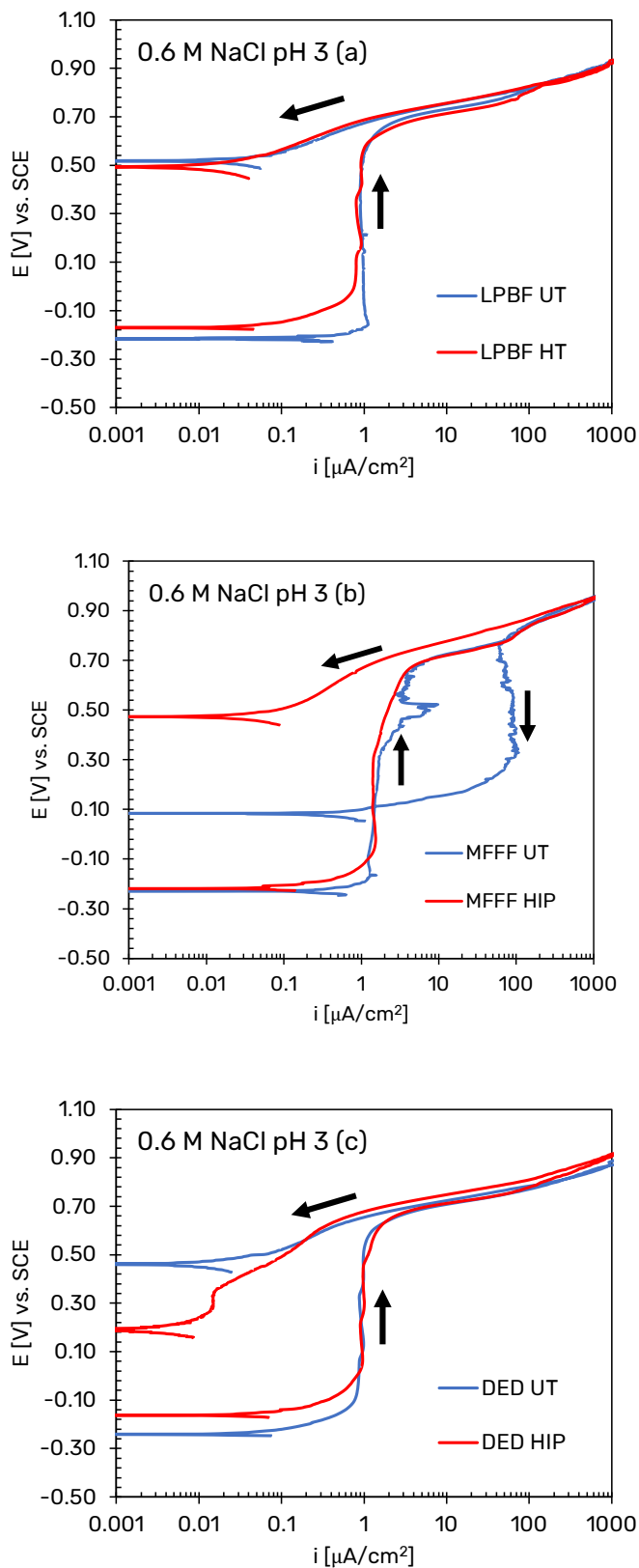


Figure 6-12: Potentiodynamic polarization curves in 0.6 M NaCl at pH 7: a) LPBF-, b) MFFF-, c) DED-manufactured samples and d) HW sample.

Figure 6-12 shows the results of cyclic potentiodynamic polarization tests in neutral chloride solution. The free corrosion potentials were lower than those obtained in the 1N H_2SO_4 solution. Moreover, in this case a higher E_{corr} was observed for the HW specimen (Figure 6-12d). The anodic polarization curves showed a wide range of passivity that ended at potential values equal to about 0.4 V vs SCE. This value is lower than the oxygen development potential, indicating the dissolution of the alloy under transpassive conditions. No differences were found in the value of anodic current density in the passivity range.

However, by reversing the scanning, the absence of a hysteresis loop and a potential value at which the sign of the current density is reversed significantly higher than the initial free corrosion potential was observed. For the specimens obtained by LPBF and MFFF, there is no difference between the untreated and post-processed conditions (Figure 6-12a and Figure 6-12b). Conversely, the DED-hipped specimen showed a much lower current density reversal potential value than the untreated conditions (Figure 6-12c).

Cyclic potentiodynamic tests carried out in 0.6 M NaCl solution at pH 3 showed a free corrosion potential higher than that observed in neutral chloride solution (Figure 6-13).



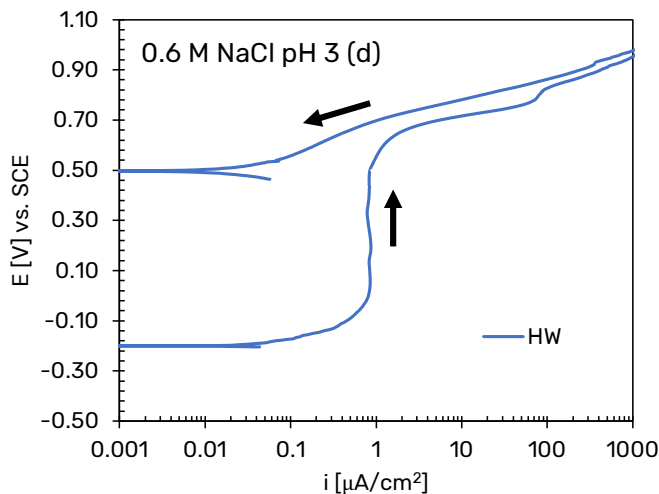


Figure 6-13: Potentiodynamic polarization curves in 0.6 M NaCl at pH 3: a) LPBF-, b) MFFF-, c) DED-manufactured samples and d) HW sample.

In this case, a difference behavior was observed. The LPBF- and DED-manufactured specimens maintain a passive behavior up to the potential of about 0.6 V vs. SCE, after which the anodic current density increases to reach the transpassivity value (Figure 6-13a and Figure 6-13c). The reverse scan curve shows a behavior without hysteresis and a potential value at which the sign of the current density is reversed slightly higher than that one observed in solution at pH 7. There again, LPBF-manufactured specimens showed no difference, while the DED-hopped specimen has a lower current density reversal potential value than the untreated conditions.

Conversely, the specimens obtained by means of MFFF show a trend like LPBF and DED only up to potential slightly higher than the free corrosion potential, beyond which a gradual increase in the anodic current density is observed (Figure 6-13b). This deviation increases as the applied potential increases, until the transpassivity potential is sharply reached.

The reverse scan curve of the MFFF-hopped specimen is similar to the HW (Figure 6-13d), showing a current density reversal potential value of about 0.5 V vs. SCE. For the untreated MFFF specimen, on the other hand, a large hysteresis and a repassivation potential of about 0.1 V vs SCE was observed in the reverse scan curve. This behavior was due to the initiation of crevice

corrosion under the gasket in correspondence with a macro defect present on the surface of the sample as shown in Figure 6-14.

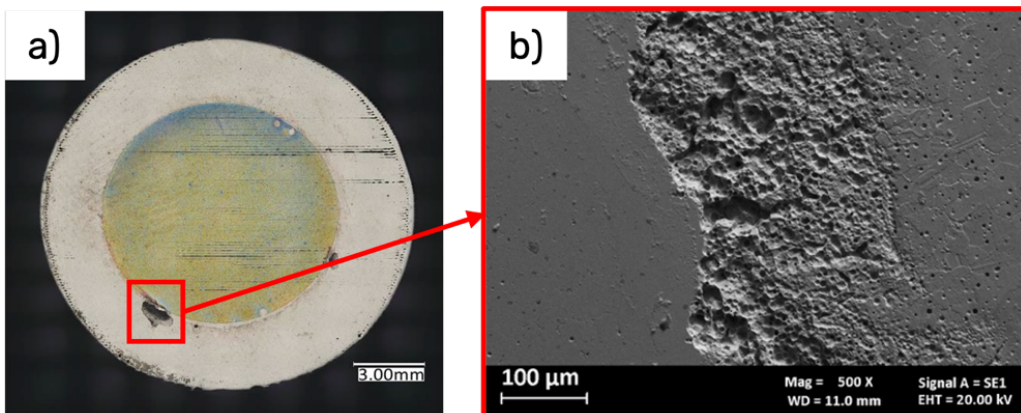
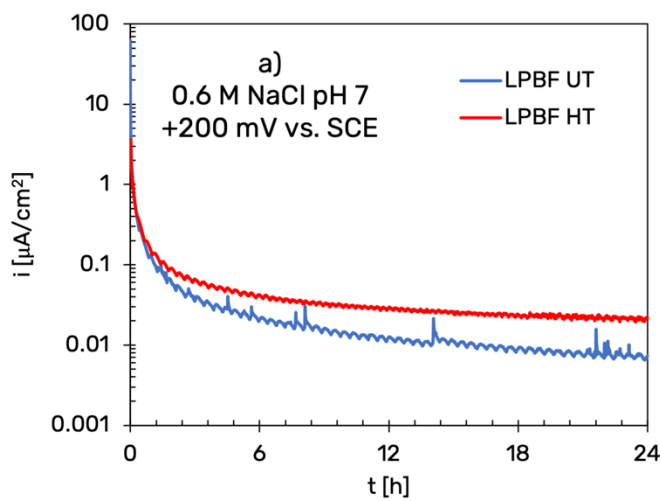


Figure 6-14: Crevice corrosion on MFFF UT specimen. a) Optical microscopy image, b) SEM image.

6.6 Potentiostatic polarization tests

The results of potentiostatic polarization tests carried out on LPBF specimens under different conditions are shown in the Figure 6-15. From the analysis of current density versus time curves, it was observed that in no case was there a rapid increase in the current density value, indicating the absence of localized corrosion attack.



Chapter 6

Results

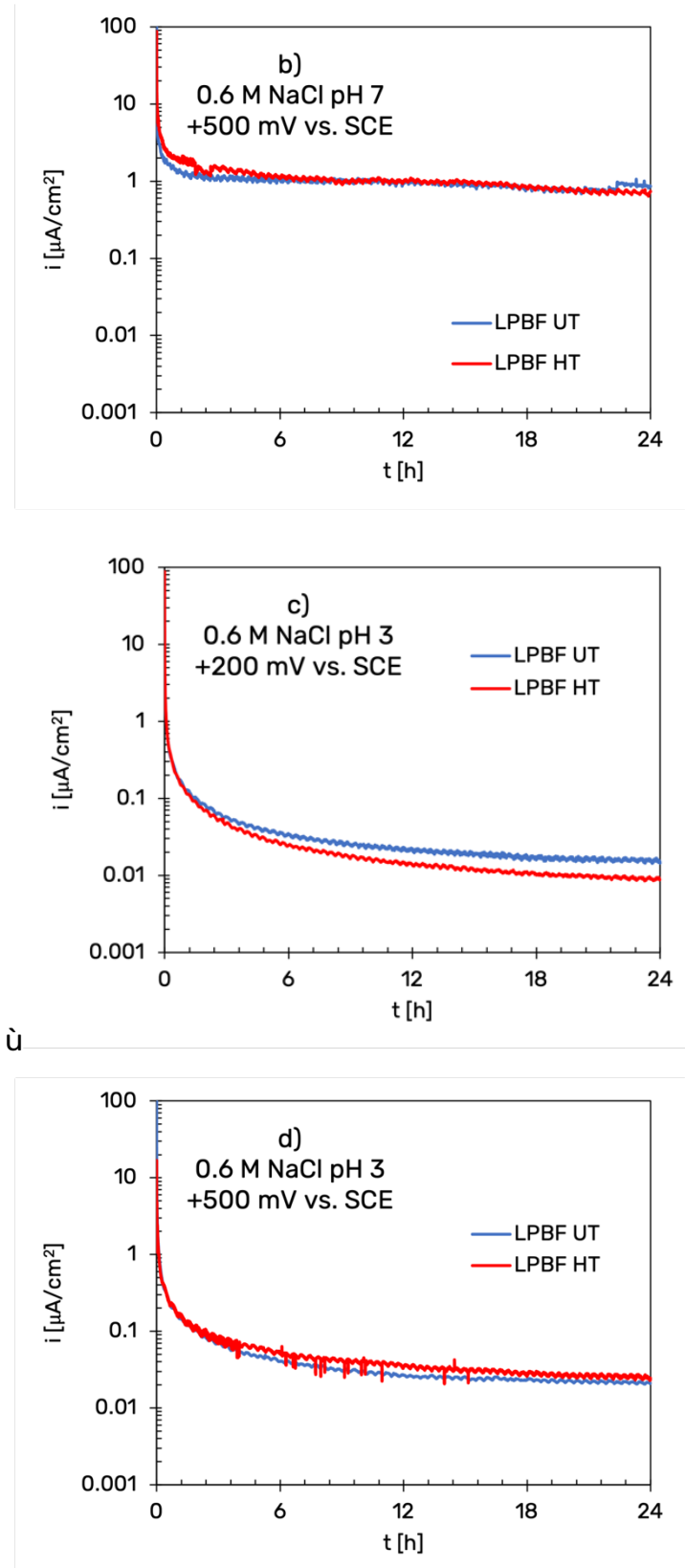


Figure 6-15: Current density vs. time during potentiostatic tests conducted on LPBF specimens a) at + 200 mV vs. SCE in 0.6M NaCl at pH7 b)) at + 500 mV vs. SCE in 0.6M NaCl at pH7 c)) at + 200 mV vs. SCE in 0.6M NaCl at pH3 d)) at + 500 mV vs. SCE in 0.6M NaCl at pH3.

During the test carried out in neutral chlorides solution at +200 mV vs SCE in Figure 6-15a, it was observed that the LPBF specimen under untreated conditions and after heat treatment reached a stable value of passive current of about 0.01 and 0.02 $\mu\text{A}/\text{cm}^2$ respectively. This value is less than the current density in the passive range i_p , evaluated in the potentiodynamic polarization curve because this test is a non-stationary technique that does not allow the passive current density to be evaluated.

For the test carried out in the same solution at +500 mV vs SCE (Figure 6-15b), the value of passive current was reached as early as one hour after the start of the test and assumes a value of about 1 $\mu\text{A}/\text{cm}^2$, which is two orders of magnitude larger than what was obtained at +200 mV vs SCE. This result confirms what was obtained by Cabrini et al [119] under the same conditions. No differences between the LPBF UT and LPBF HT were observed.

Conversely, in tests performed in acidified chloride solution, no differences were observed for LPBF UT and LPBF HT specimens between +200 and +500 mV vs. SCE (Figure 6-15c and Figure 6-15d respectively). In fact, in both cases, a stable value of passive current density of about 0.01 $\mu\text{A}/\text{cm}^2$ was reached. For the LPBF HT specimen, a slightly lower passive current density value was obtained in the test at +200 mV vs SCE compared with the untreated conditions.

The results of potentiostatic tests performed on MFFF UT and MFFF HIP specimens are shown in the Figure 6-16. Again, in none of the tests an increase in anodic current density was observed, an indication that the specimens maintain their passive behavior under these conditions.

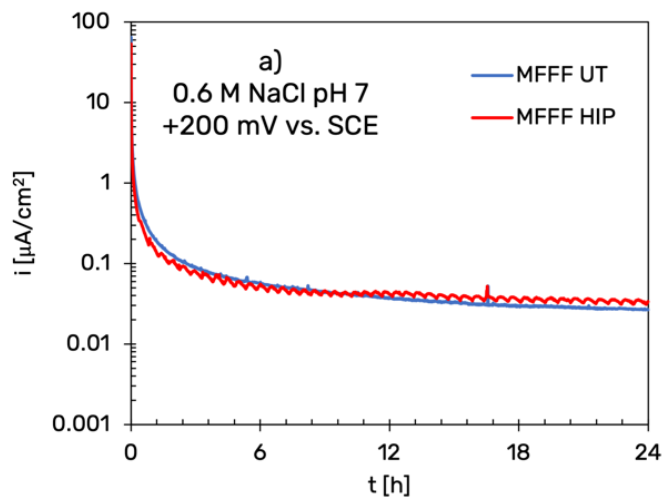
In neutral chloride solution at +200 mV vs. SCE there was no difference in behavior between the untreated conditions and after the HIP process (Figure 6-16a). Both specimens achieve a stable value of passive current density of about 0.03 $\mu\text{A}/\text{cm}^2$.

Chapter 6

Results

As in the case of the LPBF UT specimen, in the test conducted in 0.6 M NaCl solution at pH7 at +500 mV vs. SCE, the MFFF specimens reached a stable value of passive current density within one hour after the beginning of the test (Figure 6-16b). Compared with the test at +200 mV vs. SCE, in this case the MFFF UT specimen reached a slightly lower passive current density than in the hipped conditions, but which was for both about two orders of magnitude higher than those found at +200 mV vs. SCE.

No differences in behavior between untreated and hipped specimens were observed in the acidified chloride solution tests. The specimens reached a stable current density of about $0.02 \mu\text{A}/\text{cm}^2$ and $0.04 \mu\text{A}/\text{cm}^2$ in the tests carried out respectively at +200 and +500 mV vs SCE (Figure 6-16c and Figure 6-16d). The presence of many spikes of current density was observed, corresponding to the propagation and rapid repassivation of metastable pits [120].



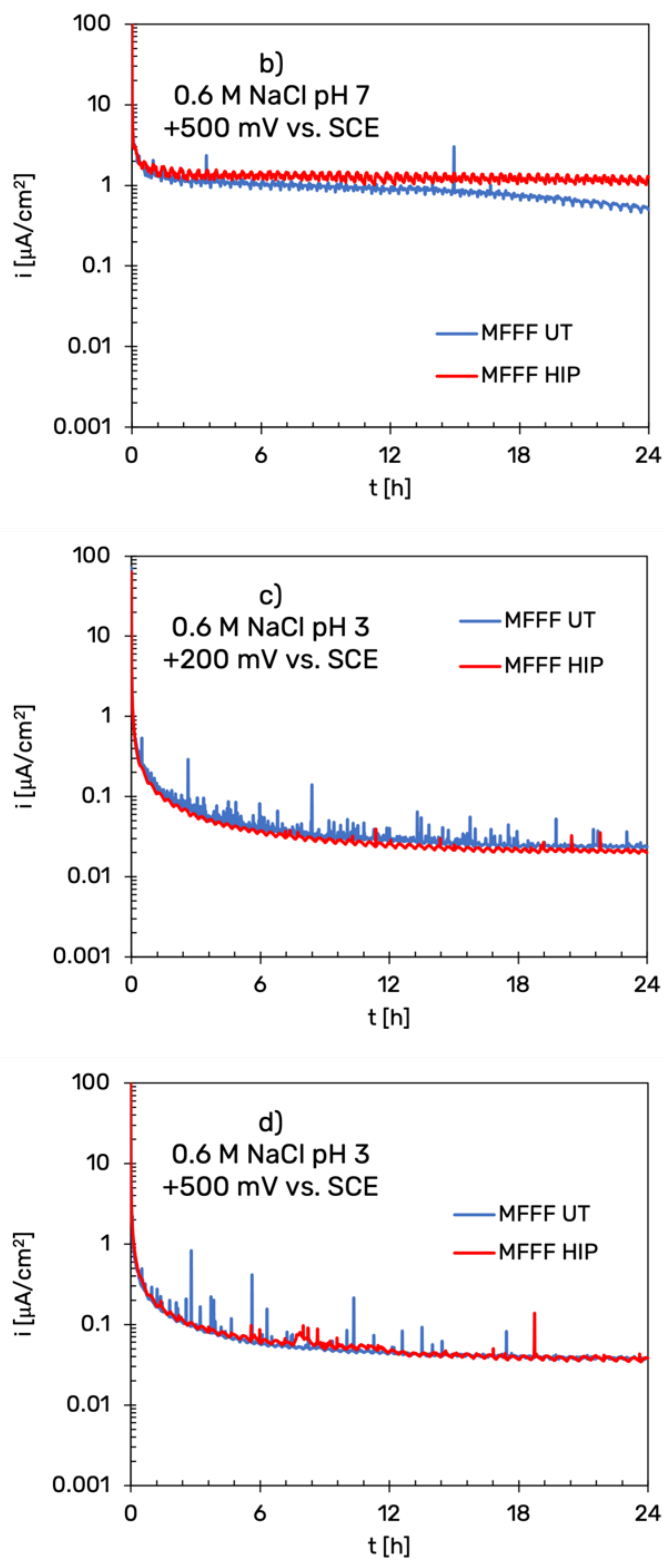


Figure 6-16: Current density vs. time during potentiostatic tests conducted on MFFF specimens a) at $+200 \text{ mV vs. SCE}$ in 0.6 M NaCl at pH 7 b) at $+500 \text{ mV vs. SCE}$ in 0.6 M NaCl at pH 7 c) at $+200 \text{ mV vs. SCE}$ in 0.6 M NaCl at pH 3 d) at $+500 \text{ mV vs. SCE}$ in 0.6 M NaCl at pH 3.

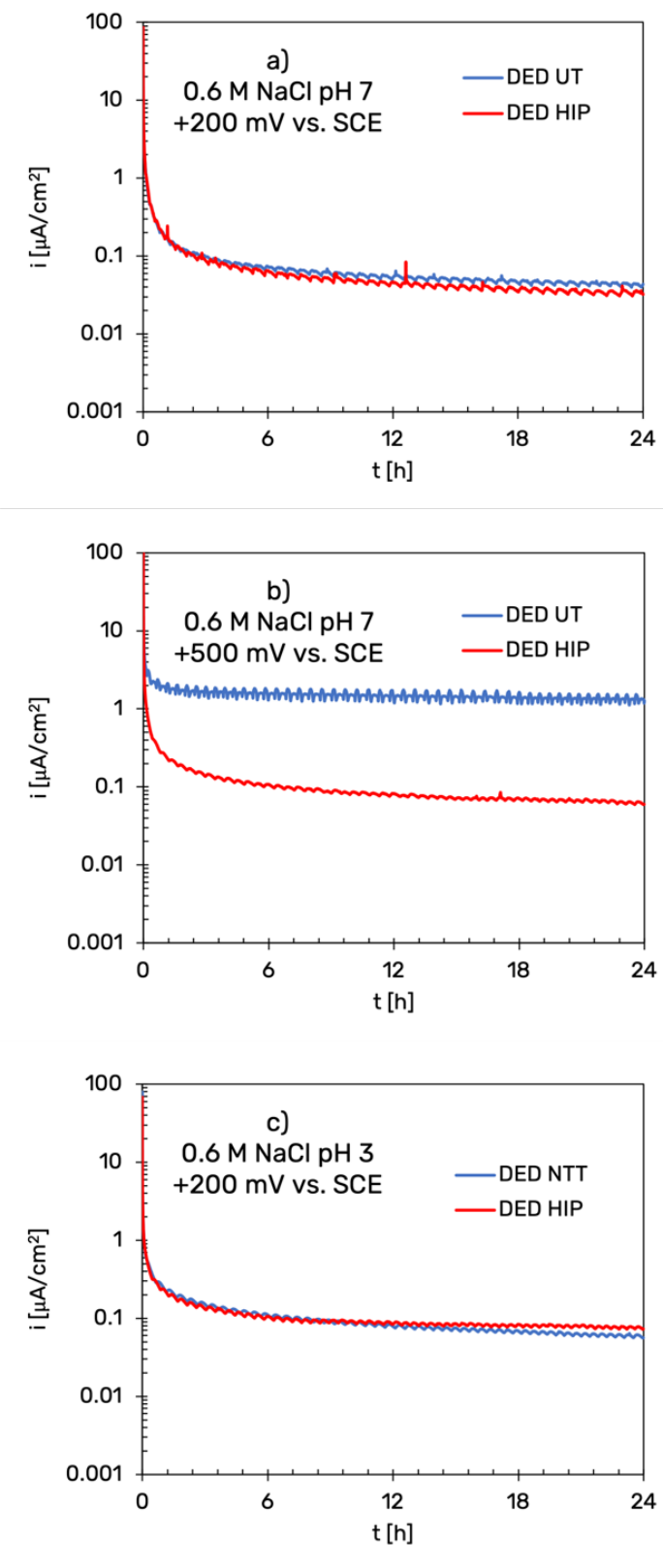
Chapter 6

Results

Finally, the Figure 6-17 shows the results of potentiostatic tests carried out on the specimens fabricated by DED technique in untreated conditions and after HIP process. As already observed for the LPBF and MFFF techniques, there was no increase in anodic current density for DED-manufactured specimens in any of the tests performed.

In neutral chloride solution at +200 mV vs SCE, the passive current density value reached a stable value of about $0.04 \mu\text{A}/\text{cm}^2$ and $0.03 \mu\text{A}/\text{cm}^2$ for DED UT and DED HIP specimens respectively (Figure 6-17a). Conversely, a different behavior was observed during the test performed at +500 mV vs SCE between the two conditions (Figure 6-17b). In fact, the untreated DED specimen quickly reaches an anode current density value of about $1.3 \mu\text{A}/\text{cm}^2$, while the hipped specimen reached more slowly a value of 0.06, which is two orders of magnitude lower.

In 0.6 M NaCl at pH 3 the anodic current density curves versus time of DED specimens showed very similar behavior. At +200 mV vs SCE (Figure 6-17c) DED UT and DED HIP specimen reached a passive current density of $0.06 \mu\text{A}/\text{cm}^2$ and $0.07 \mu\text{A}/\text{cm}^2$ respectively. Slightly higher values were achieved in the test at + 500 mV vs SCE (Figure 6-17d) in which the UT specimen reached an anodic current density of $0.09 \mu\text{A}/\text{cm}^2$, while the HIP-processed specimen reached $0.08 \mu\text{A}/\text{cm}^2$.



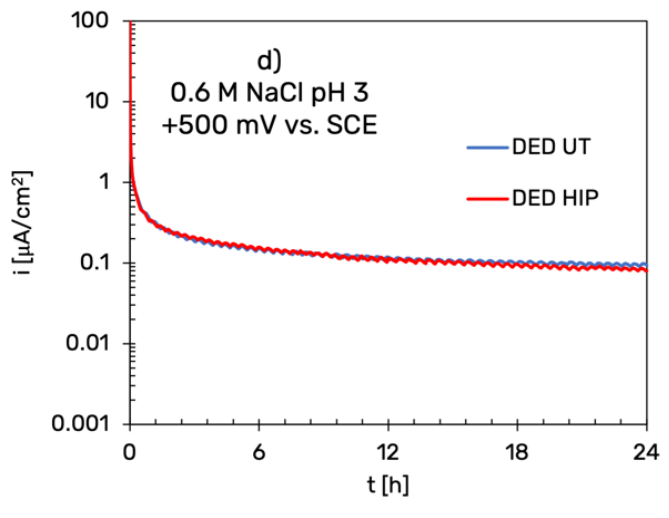


Figure 6-17: Current density vs. time during potentiostatic tests conducted on DED specimens a) at + 200 mV vs. SCE in 0.6M NaCl at pH7 b) at + 500 mV vs. SCE in 0.6M NaCl at pH7 c) at + 200 mV vs. SCE in 0.6M NaCl at pH3 d) at + 500 mV vs. SCE in 0.6M NaCl at pH3.

6.7 Hardness tests

The average low force Vickers hardness was evaluated for all the AM-processed specimens, providing the values reported in Figure 6-18. The specimens manufactured via LPBF resulted in the highest hardness values, mainly due to the very small size on the dendritic regions. These were slightly larger in the DED-produced specimens, leading to a decrease in terms of hardness. Finally, these structures were completely absent in the MFFF-processed material, characterized by far by the lowest hardness (189 ± 11 HV). post-processing treatment on the LPBF and DED specimens leads to a decrease in hardness value, while in the case of MFFF, which is characterized by a finer grain structure, an increase in hardness was observed.

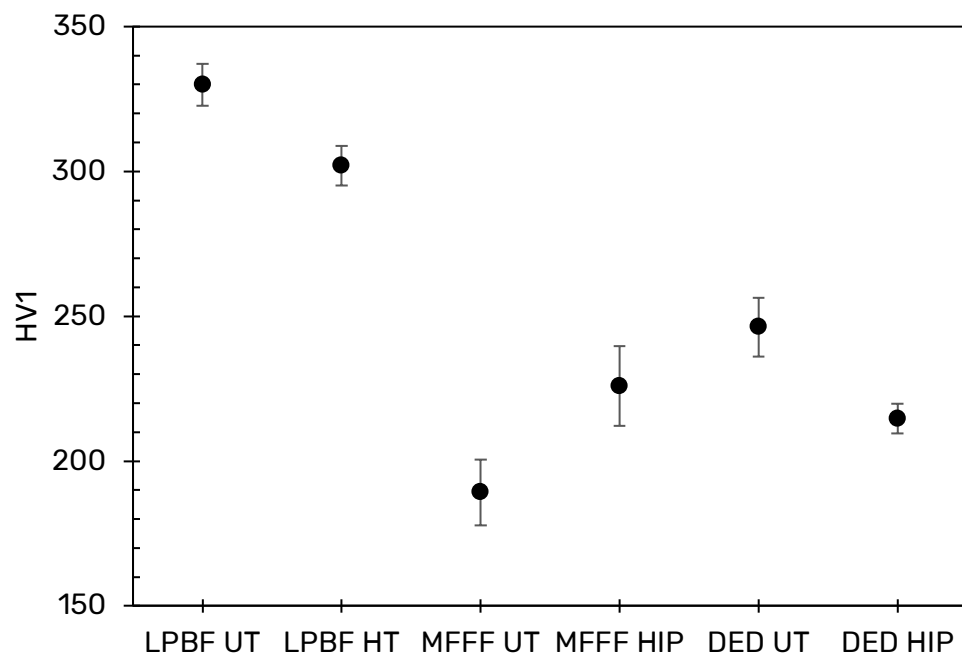


Figure 6-18: Outcome of the low force Vickers hardness test for the AM-processed specimens.

DISCUSSION

7.1 Defect analysis on MFFF-manufactured specimens

From the porosity analysis performed on the specimens obtained by AM technologies, it was observed that the MFFF technology is characterized by porosity values two orders of magnitude higher than those of the DED and LPBF techniques.

The defects observed on the cross section are different in nature. The presence of micro- pores randomly distributed throughout the whole cross section might be attributed to pre-existing gas porosities in the feedstock powder and/or the sintering step.

Conversely, macro defects are characterized by a periodic distribution with a distance equal to about the thickness of a deposited layer. Therefore, it is reasonable to assume that the macro-defects were created in correspondence of the area where two stripes met during the deposition phase. This remark is further corroborated by the shape of this defects. This was an upward facing triangle in the core, possibly resulting by the conjunction of a scan parallel to the metallographic section, and two perpendicular scans of the upper scan layer (Figure 7-1a, b). In fact, the scanning strategy adopted implemented a 90° rotation between successive layers. Conversely, the macro-defects found in the contour were

characterized by a quadrilateral shape, due to the different scanning strategy adopted in this area. In fact, no rotation was set to occur when moving to a successive layer, as visible in Figure 7-1c. It is also worth mentioning that these voids appeared more elongated. A possible explanation lies in the cross-sectioning direction, which was perpendicular to the scanning lines in the core, but 45°-oriented with respect to the ones in the contour.

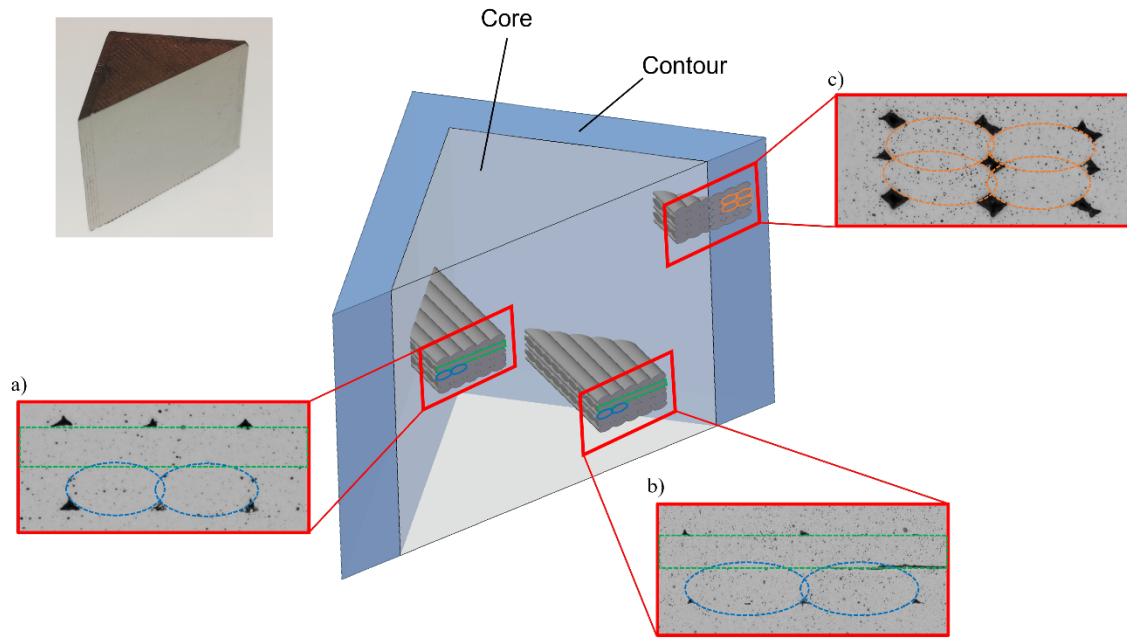


Figure 7-1: Representative view of the wire scan directions and their correspondence with the locations of a),b) the triangular macro-defects in the core and c)quadrilateral macro-defects in the contour). The green, blue, and orange dashed lines represent respectively the parallel, perpendicular, and 45°-oriented wire scan lines, with respect to the cross-section plane. The sizes represented were altered on purpose to improve the readability.

Micro-pores and interlayer voids were also assessed in other works. Thomas and Gleadall [91] described interlayer defects as intentional. In fact, according to these authors, these voids should coalesce and disappear during sintering. However, these were still clearly visible in the fracture surfaces of the post-sintered specimens showed in their work. Costa et al. [90] attributed these defects with the under extrusion of the filament during deposition, or a sub-optimal optimization of the parameters.

To sum up, micro-pores can be considered intrinsic defects, caused by the quality of the feedstock material and debinding phase. Conversely, the

macro-pores can be categorized as extrinsic defects, generated by the scanning strategy adopted.

The cross-sectional pore size was estimated by evaluating the equivalent diameter (D_{EQ}), using the following equation:

$$D_{EQ} = 2 \sqrt{\frac{A}{\pi}} \quad \text{Eq. 5-1}$$

Where A is the area occupied by a given pore, obtained via digital image analysis. The resulting analysis, provided in Figure 7-2a, describes a bimodal size distribution of the defects, characterized by a primary peak at 5 μm (micro-pores) and a secondary peak at 30 μm (macro-defects). The threshold between micro- and macro-defects was determined by carefully comparing a relevant (≈ 50) number of pores randomly selected in each class of the distribution. This value was found at 20 μm , which corresponds to the local minimum of the distribution. The pore aspect ratio (AR) was evaluated as well, using the following equation:

$$AR = \frac{d_{Feret}}{d_{Feret,min}} \quad \text{Eq. 5-2}$$

Where $d_{Feret,min}$ represents the minimum Feret's diameter. The vast majority of the defects in the material were characterized by an AR >0.5 , as provided in Figure 7-2b. These pores can be considered quasi-spherical and are characterized by a comparatively smaller size. Lower AR values are achieved by defects progressively bigger (e.g., elongated).

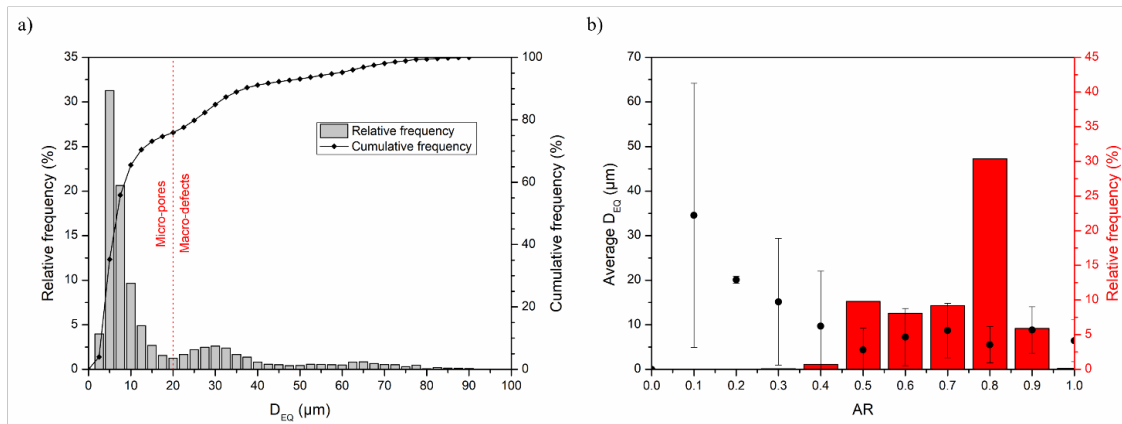


Figure 7-2: a) Pore size distribution and b) pore aspect ratio distribution and correlation with size by image analysis of the optical micrographs of the MFFF-processed samples.

The image analyses performed on the cross-section of the MFFF-processed specimens highlighted the presence of a relevant number of directional macro-defects, whose cross-section analyses might be misleading due to possible underestimations of their overall volume, as these voids might achieve lengths comparable to the size of the specimen itself. This effect was suggested by the presence of sparse elongated defects in the cross-section.

7.2 Selective corrosion behavior

To investigate the different behaviors observed on MFFF specimens associated with high corrosion rate compared with LPBF and DED specimens, local microstructural variations were investigated. In the core part, the Mo-, Nb- and Si-rich precipitates provided a blocky morphology. These phases were mainly located at the grain boundaries and secondly in correspondence of the oxidized areas and center of the grains (Figure 7-3a). Their presence was also found on the inner surface of the elongated macro-defects (Figure 7-3c). The relative volume fraction was 3.2%. Instead, the secondary phase found in the contour part was characterized by an elongated morphology, clearly following the grain boundaries borders (Figure 7-3b). Moreover, its presence was also detected on the inner surface of the elongated macro-defects (Figure 7-3d). The relative volume fraction was 1.0%.

It is worth mentioning that the MFFF-produced samples had a higher C content with respect to the all the other conditions. Whether carbon pick-up

occurred during the sintering phase, due to the decomposition of the residual binder, is still unclear. However, similar phenomena were reported by other authors. For instance, Thompson et al. [116] declared that an increase in carbon content, causing carbides formation, occurred in MFFF-produced alloy 718.

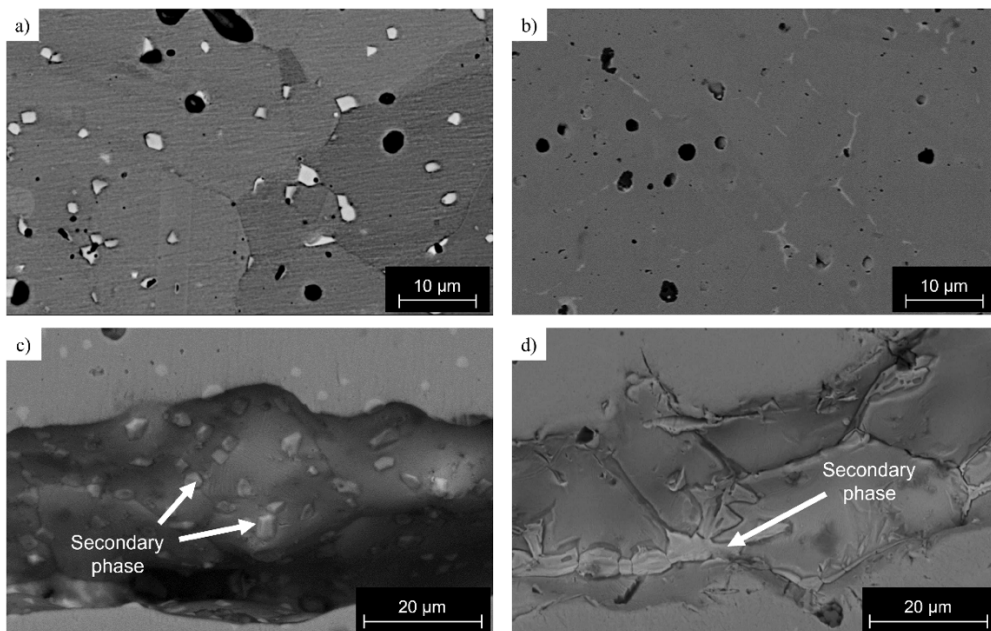


Figure 7-3: Different microstructural features in the microstructure (a,b) and inside the elongated macro-defects (c,d) in the core and contour of the MFFF-produced alloy 625, respectively.

This is mainly linked to the thermal decomposition of the binder during the debinding and sintering steps. The shape, length and width of the open channels might determine how easily the decomposition byproducts escape and/or permeate the material. Therefore, it can be assumed that the different scanning strategies adopted influence the ability of the byproducts of the polymer decomposition to leave the specimens, thus influencing the local microstructure of the material. This seems to be confirmed by the increased C content in the secondary phases and their frequent localization in correspondence of the edge of the defects.

In general, the precipitation of secondary phases might induce a degradation of the corrosion resistance in Ni alloys [121]. This effect is mostly due to the relative depletion of some elements from the matrix (γ), which results in an

increase susceptibility to intergranular corrosion. For example, Mo depletion is a well-known cause for preferential corrosion [122]. Considering binder jetting, another AM technology relying on a polymeric binder, Mostafaei et al. [123] reported massive carbides formation, causing significant Mo, Nb and Cr depletion in large areas. It is also worth considering that the precipitates in the core appeared larger and more frequent than those in the contour, suggesting a more intense element depletion from the Ni matrix. Hence, the higher susceptibility to corrosion in the core portion of the material was probably due to a more significant depletion of protecting elements (Mo, Nb) from the surrounding grains. In general, the corrosion follows the microstructural features highlighted in the MFFF-manufactured alloy 625. Furthermore, the material provided local morphological phase variations that were reflected by a different behavior of the core and contour portions during the susceptibility to intergranular corrosion test.

7.1 Localized corrosion behavior

Localized corrosion behavior was evaluated by potentiodynamic and potentiostatic polarization tests. Figure 7-4 shows the free corrosion potential (E_{corr}) of alloy 625 obtained by AM and conventional techniques for different test solutions.

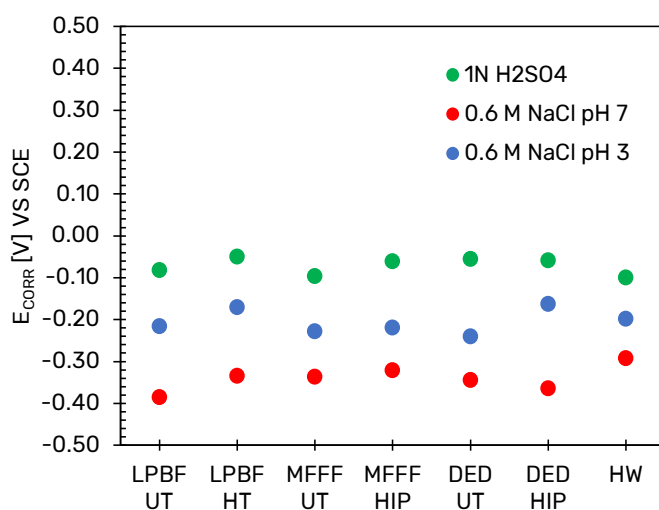


Figure 7-4: E_{corr} of Alloy 625 obtained by means of AM and traditional technology in different test solutions.

It was generally observed that, regardless of the production technique, E_{corr} is lower in neutral than in acidified chloride solution, while the highest, i.e., nobler potential values were achieved in 1N H_2SO_4 . This is associated with the nobility of the cathodic oxygen reduction process, which increases as the pH value decreases.

Particularly, the specimens obtained by LPBF and MFFF after post-processing treatment showed slightly higher E_{corr} than the untreated conditions in all solutions. Conversely, the specimens obtained by DED technique had a different behavior. In 1N H_2SO_4 solution, there were no differences between the hipped and untreated conditions. In acidified chloride solution, DED post-processed specimen reached a E_{corr} value higher than the untreated conditions, while in neutral chloride solution, the untreated specimen showed a higher E_{corr} value.

The potential at which a rapid growth of anodic current density was observed may be due, in addition to initiation of crevice attack, to two phenomena, namely, the attainment of transpassivity potential E_t with consequent dissolution of the material, or the oxygen evolution reaction (OER). In the case of crevice corrosion attack, the potential versus current density curve shows a hysteresis loop when the scan is reversed, while the distinction between E_t and OER can be made on a thermodynamic basis by calculating the OER via the Nernst equation. Figure 7-5 shows that regardless of the production technology of alloy 625, the values of the potentials corresponding to the rapid increase in anodic current density are slightly lower than the OER potential in both 1N H_2SO_4 and chloride solutions. Generally, a decrease in E_t potential value was observed as pH increased. Particularly, in 1N H_2SO_4 solution the HW specimen and AM-manufactured specimens both under untreated conditions (Figure 7-5a) and after post processing treatment (Figure 7-5b) are characterized by the same transpassivity potential. Conversely, differences were observed in chloride solutions, with a general trend of slight decrease in transpassivity potential for AM-treated specimens compared with specimens under untreated conditions. Moreover, among the

different AM technologies, MFFF-manufactured specimens are characterized by higher E_t than specimens obtained by means of LPBF and DED.

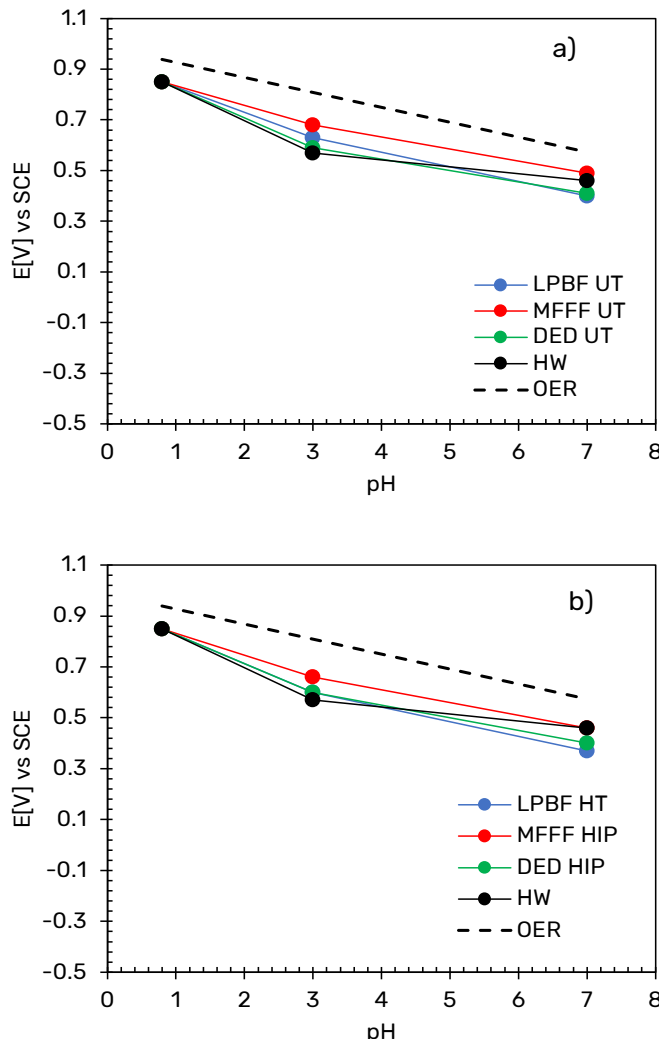


Figure 7-5: Transpassive potential (E_t) as a function of pH for a) AM-fabricate specimens in untreated conditions and b) AM-manufactured specimen after post-processing treatment compared with the HW.

It is worth noting that in the acidified chloride solution, although the untreated MFFF samples showed a wide range of passive behavior, they did undergo crevice attack. In this case, as reported by Cabrini et al [119], crevice attack occurred at high potential values that are not reached under normal operating conditions, that is, under conditions in which acidification and oxidation of chromium oxide associated with OER promote localized attack.

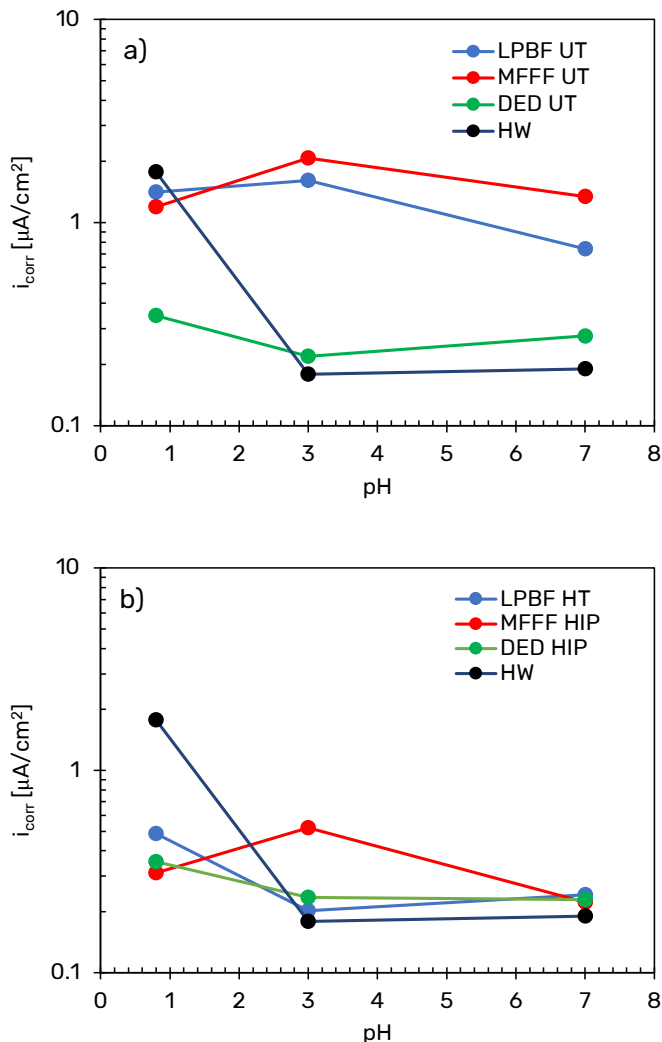


Figure 7-6: Corrosion current density as a function of pH for a) AM-fabricate specimens in untreated conditions and b) AM-manufactured specimen after post-processing treatment compared with the HW.

The corrosion current density i_{corr} was evaluated by the Stern-Geary equation 7-1:

$$i_{corr} = \frac{B}{R_p} \quad \text{Eq. 7-1}$$

Where:

- B is a constant that typically takes the value of 52 mV/decade for a material with passive behavior
- R_p is the polarization resistance evaluated in the range of ± 10 mV with respect to E_{corr} .

The results in the Figure 7-6 show that the post-processed AM specimens and in particular those obtained by MFFF and LPBF are characterized by a lower corrosion current density (Figure 7-6b) compared to the untreated conditions (Figure 7-6a).

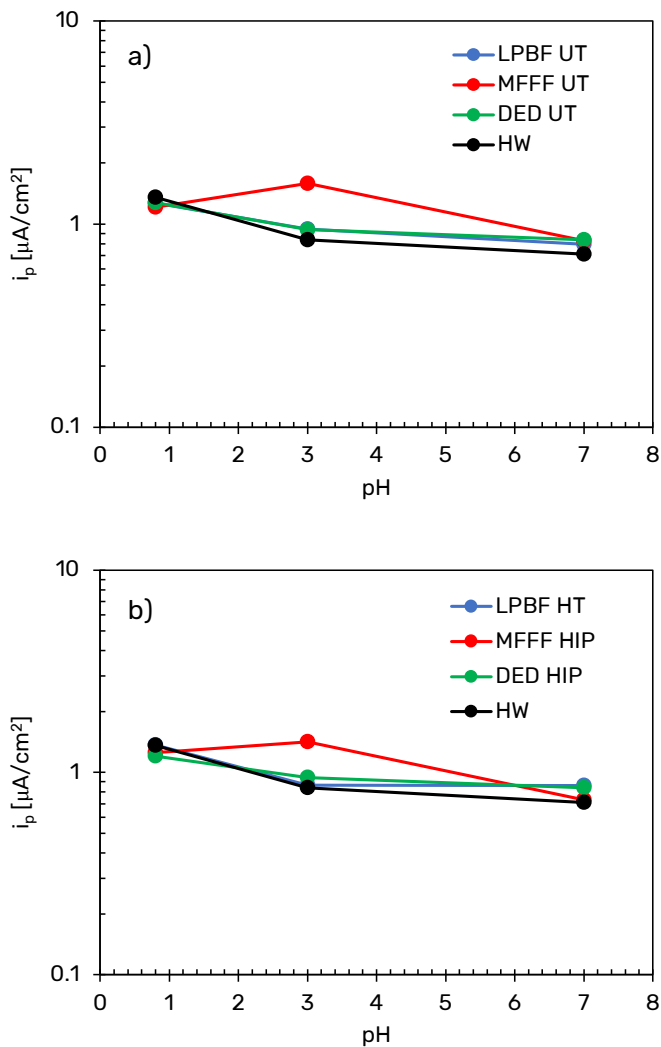


Figure 7-7: Corrosion current density in the passive range as a function of pH for a) AM-fabricate specimens in untreated conditions and b) AM-manufactured specimen after post-processing treatment compared with the HW.

Finally, the current density in the passivity range was also evaluated. The results in the Figure 7-7 show that, except for the specimens obtained by MFFF, the current density in the passive range decreases slightly as the pH value increases. The difference between i_p of untreated (Figure 7-7a) and post-processed (Figure 7-7b) LPBF- and DED-manufactured specimens compared to HW specimens is negligible in all test solutions. Similar results

were also obtained on MFFF-manufactured specimens both in sulfuric acid and neutral chlorides solution, while in acidified chloride solution an increase in the i_p value was observed both in untreated conditions and after the HIP process.

To sum up, in the potentiodynamic polarization tests performed, all specimens showed a passive behavior, with no localized attacks, except for the untreated MFFF specimens in acidified chloride solution in which crevice corrosion was observed under the gasket.

Potentiostatic polarization tests were also carried out to investigate localized corrosion behavior. None of the tested specimens suffered a pitting or crevice corrosion attack. Therefore, the results obtained showed that the alloy 625 specimens obtained by means of AM techniques has a similar corrosion behavior, if not better than the same alloy obtained through conventional techniques.

CONCLUSION

This PhD thesis presents the results of the experimental activity conducted on the nickel-based alloy 625 obtained by means of different additive manufacturing (AM) technologies, namely Laser Powder Bed Fusion (LPBF), Directed Energy Deposition (DED) and Metal Fused Filament Fabrication (MFFF).

The specimens produced by AM have been studied in terms of defectology, microstructure, hardness, and corrosion behavior. Particularly, intergranular corrosion susceptibility and localized corrosion resistance have been assessed, comparing the results with an alloy of similar chemical composition obtained by traditional processing techniques. In addition, the effect of a post process treatment on the corrosion behavior of the AM-produced specimens was evaluated.

The LPBF and DED-processed specimens provided very low porosity values, confirming that these technologies are currently well established and the relative process parameters are optimized. Conversely, the specimens produced by MFFF process were characterized a significant number of defects. In the MFFF-processed material were found small pores, both pre-existing in the feedstock material and generated during the debinding phase. Moreover, periodically distributed elongated macro-defects, result of the scanning strategy adopted, were also detected.

The LPBF- and DED -built specimens provided a microstructure coherent with the existing literature. Conversely, MFFF-processed material was characterized by equiaxed γ grains with Mo-, Nb- and Si- rich second phases. These provided a blocky morphology in the core and an elongated shape in the contour region.

The highest hardness was provided by the samples manufactured via LPBF. The DED-processed material had a lower value, due to the coarser dendritic microstructure. Instead, the MFFF-built specimens were characterized by the lowest hardness, due to the complete disappearance of the dendritic structure.

Intergranular corrosion test showed that in general the specimens obtained by AM techniques, both under untreated conditions and after post-processing treatments, were characterized by lower corrosion rates than the material obtained by conventional processes. However, while the LPBF and DED specimens did not show any significant attacks, the MFFF specimens showed a different behavior in the contour region, on which the selective attacks were negligible, and the core of the specimen in which the presence of penetrating attacks was observed. This therefore confirms that corrosion behavior is strictly dependent on production technology and process parameters.

Potentiodynamic tests in sulfuric acid showed that AM specimens are characterized by a behavior like the traditional material, showing a wide range of passive behavior of the material, thus confirming the excellent corrosion resistance in this environment.

Finally, cyclic potentiodynamic and potentiostatic polarization tests in chloride solution showed that the specimens obtained by LPBF and DED have a similar, if not higher, resistance to localized corrosion than traditional material. Conversely, the alloy obtained by MFFF under untreated conditions showed crevice corrosion in acidified solution, while after hot isostatic pressing treatment, the material did not undergo corrosion attacks.

REFERENCES

- [1] G.R. Thellaputta, P.S. Chandra, C.S.P. Rao, Machinability of Nickel Based Superalloys: A Review, Mater Today Proc. 4 (2017) 3712–3721. <https://doi.org/10.1016/J.MATPR.2017.02.266>.
- [2] G.M. Volpato, U. Tetzlaff, M.C. Fredel, A comprehensive literature review on laser powder bed fusion of Inconel superalloys, Addit Manuf. 55 (2022). <https://doi.org/10.1016/J.ADDMA.2022.102871>.
- [3] Z.F. Yin, W.Z. Zhao, W.Y. Lai, X.H. Zhao, Electrochemical behaviour of Ni-base alloys exposed under oil/gas field environments, Corros Sci. 51 (2009) 1702–1706. <https://doi.org/10.1016/J.CORSCI.2009.04.019>.
- [4] J.K. Brownlee, K.O. Flesner, K.R. Riggs, B.P. Miglin, Selection and Qualification of Materials for HPHT Wells, Society of Petroleum Engineers - SPE High Pressure/High Temperature Sour Well Design Applied Technology Workshop 2005, HPHT 2005. (2005). <https://doi.org/10.2118/97590-MS>.
- [5] M.B. Henderson, D. Arrell, R. Larsson, M. Heobel, G. Marchant, Nickel based superalloy welding practices for industrial gas turbine applications,

- <Https://Doi.Org/10.1179/136217104225017099>. 9 (2013) 13–21.
<https://doi.org/10.1179/136217104225017099>.
- [6] V. Shankar, K. Bhanu Sankara Rao, S.L. Mannan, Microstructure and mechanical properties of Inconel 625 superalloy, *Journal of Nuclear Materials.* 288 (2001) 222–232.
[https://doi.org/10.1016/S0022-3115\(00\)00723-6](https://doi.org/10.1016/S0022-3115(00)00723-6).
- [7] S. Li, Q. Wei, Y. Shi, C.K. Chua, Z. Zhu, D. Zhang, Microstructure Characteristics of Inconel 625 Superalloy Manufactured by Selective Laser Melting, *J Mater Sci Technol.* 31 (2015) 946–952.
<https://doi.org/10.1016/J.JMST.2014.09.020>.
- [8] H.M. Tawancy, I.M. Allam, N.M. Abbas, Effect of Ni₃Nb precipitation on the corrosion resistance of Inconel alloy 625, *J Mater Sci Lett.* 9 (1990) 343–347.
<https://doi.org/10.1007/BF00725845>.
- [9] P. Kritzer, N. Boukis, E. Dinjus, Review of the corrosion of nickel-based alloys and stainless steels in strongly oxidizing pressurized high-temperature solutions at subcritical and supercritical temperatures, *Corrosion.* 56 (2000) 1093–1104.
<https://doi.org/10.5006/1.3294394>.
- [10] M. Shahwaz, P. Nath, I. Sen, A critical review on the microstructure and mechanical properties correlation of additively manufactured nickel-based superalloys, *J Alloys Compd.* 907 (2022) 164530.
<https://doi.org/10.1016/J.JALCOM.2022.164530>.
- [11] M. Karmuhilan, S. Kumanan, A Review on Additive Manufacturing Processes of Inconel 625, (2019).
<https://doi.org/10.1007/s11665-021-06427-3>.
- [12] Y. Tian, N. Chekir, X. Wang, A. Nommeots-Nomm, R. Gauvin, M. Brochu, Microstructure characterization and grain morphology of

- alloy 625 with 0.4 wt% boron modification manufactured by laser wire deposition, Addit Manuf. 24 (2018) 137–144. <https://doi.org/10.1016/j.addma.2018.09.015>.
- [13] ASTM International, ASTM B443-19: Standard Specification for Nickel-Chromium-Molybdenum-Columbium Alloy and Nickel-Chromium-Molybdenum-Silicon Alloy Plate, Sheet, and Strip, (2019). <https://www.astm.org/b0443-19.html>.
- [14] N. Jeyaprakash, C.H. Yang, S.S. Karuppasamy, S.R. Dhineshkumar, Evaluation of microstructure, nanoindentation and corrosion behavior of laser cladded Stellite-6 alloy on Inconel-625 substrate, Mater Today Commun. 31 (2022) 103370. <https://doi.org/10.1016/J.MTCOMM.2022.103370>.
- [15] G.F. vander Voort, G.M. Lucas, E.P. Manilova, Metallography and Microstructures of Heat-Resistant Alloys, Metallography and Microstructures. (2004) 820–859. <https://doi.org/10.31399/ASM.HB.V09.A0003737>.
- [16] F. Masoumi, D. Shahriari, M. Jahazi, J. Cormier, A. Devaux, Kinetics and Mechanisms of γ' Reprecipitation in a Ni-based Superalloy, Scientific Reports 2016 6:1. 6 (2016) 1–16. <https://doi.org/10.1038/srep28650>.
- [17] S. Floreen, G.E. Fuchs, W.J. Yang, The Metallurgy of Alloy 625, (n.d.).
- [18] Y.L. Hu, X. Lin, X.B. Yu, J.J. Xu, M. Lei, W.D. Huang, Effect of Ti addition on cracking and microhardness of Inconel 625 during the laser solid forming processing, J Alloys Compd. 711 (2017) 267–277. <https://doi.org/10.1016/J.JALLOCOM.2017.03.355>.
- [19] W.E. Frazier, Metal additive manufacturing: A review, J Mater Eng Perform. 23 (2014). <https://doi.org/10.1007/s11665-014-0958-z>.

- [20] J.P. Kruth, M.C. Leu, T. Nakagawa, Progress in additive manufacturing and rapid prototyping, CIRP Ann Manuf Technol. 47 (1998). [https://doi.org/10.1016/S0007-8506\(07\)63240-5](https://doi.org/10.1016/S0007-8506(07)63240-5).
- [21] D.D. Gu, W. Meiners, K. Wissenbach, R. Poprawe, Laser additive manufacturing of metallic components: materials, processes and mechanisms, <Https://Doi.Org/10.1179/1743280411Y.0000000014>. 57 (2013) 133–164. <https://doi.org/10.1179/1743280411Y.0000000014>.
- [22] M. Yakout, M.A. Elbestawi, S.C. Veldhuis, A review of metal additive manufacturing technologies, Solid State Phenomena. 278 SSP (2018) 1–14. <https://doi.org/10.4028/www.scientific.net/ssp.278.1>.
- [23] A. Bandyopadhyay, K.D. Traxel, M. Lang, M. Juhasz, N. Eliaz, S. Bose, Alloy design via additive manufacturing: Advantages, challenges, applications and perspectives, Materials Today. 52 (2022) 207–224. <https://doi.org/10.1016/J.MATTOD.2021.11.026>.
- [24] V. Madhavadas, D. Srivastava, U. Chadha, A. Raj, M. Thariq, H. Sultan, F. Syazwani Shahar, A. Umaira, M. Shah, A review on metal additive manufacturing for intricately shaped aerospace components, (2022). <https://doi.org/10.1016/j.cirpj.2022.07.005>.
- [25] T. Pichler, J.H. Schleifenbaum, Examination of the LPBF Process by Means of Thermal Imaging for the Development of a Geometric-specific Process Control, (n.d.).
- [26] A. Khorasani, I. Gibson, J. Kozhuthala Veetil, & Amir, H. Ghasemi, A review of technological improvements in laser-based powder bed fusion of metal printers, (n.d.). <https://doi.org/10.1007/s00170-020-05361-3>.
- [27] S. Cao, Y. Zou, C.V.S. Lim, X. Wu, Review of laser powder bed fusion (LPBF) fabricated Ti-6Al-4V: process, post-process treatment,

- microstructure, and property, Light: Advanced Manufacturing. 2 (2021) 1. <https://doi.org/10.37188/LAM.2021.020>.
- [28] A.N. Jinoop, C.P. Paul, K.S. Bindra, Laser-assisted directed energy deposition of nickel super alloys: A review, <Https://Doi.Org/10.1177/1464420719852658>. 233 (2019) 2376–2400. <https://doi.org/10.1177/1464420719852658>.
- [29] A. Dass, A. Moridi, State of the Art in Directed Energy Deposition: From Additive Manufacturing to Materials Design, Coatings 2019, Vol. 9, Page 418. 9 (2019) 418. <https://doi.org/10.3390/COATINGS9070418>.
- [30] A. Carrozza, F. Mazzucato, A. Aversa, M. Lombardi, F. Bondioli, S. Biamino, A. Valente, P. Fino, Single Scans of Ti-6Al-4V by Directed Energy Deposition: A Cost and Time Effective Methodology to Assess the Proper Process Window, Metals and Materials International. 27 (2021) 3590–3602. <https://doi.org/10.1007/S12540-020-00930-3/FIGURES/11>.
- [31] P. Singh, V.K. Balla, A. Tofangchi, S. v. Atre, K.H. Kate, Printability studies of Ti-6Al-4V by metal fused filament fabrication (MF3), Int J Refract Metals Hard Mater. 91 (2020) 105249. <https://doi.org/10.1016/J.IJRMHM.2020.105249>.
- [32] Y. Thompson, J. Gonzalez-Gutierrez, C. Kukla, P. Felfer, Fused filament fabrication, debinding and sintering as a low cost additive manufacturing method of 316L stainless steel, Addit Manuf. 30 (2019) 100861. <https://doi.org/10.1016/J.ADDMA.2019.100861>.
- [33] V.B. Nidagundi, R. Keshavamurthy, C.P.S. Prakash, Studies on Parametric Optimization for Fused Deposition Modelling Process, Mater Today Proc. 2 (2015) 1691–1699. <https://doi.org/10.1016/J.MATPR.2015.07.097>.

- [34] M.T. Rahman, R. Panat, Aerosol jet 3D printing and high temperature characterization of nickel nanoparticle films, *Manuf Lett.* 29 (2021) 5–10. <https://doi.org/10.1016/J.MFGLET.2021.04.006>.
- [35] H.O. Коваль, О.С. Воденникова, INVESTIGATION OF MECHANICAL PROPERTIES AND STRUCTURE OF IN718 ALLOY PRODUCED BY 3D-PRINTING, *Aerospace Technic and Technology.* 0 (2020) 21–29. <https://doi.org/10.32620/AKTT.2020.3.03>.
- [36] W. Abd-Elaziem, S. Elkataatny, A.-E. Abd-Elaziem, M. Khedr, M.A. Abd El-baky, M.A. Hassan, M. Abu-Okail, M. Mohammed, A. Järvenpää, T. Allam, A. Hamada, On the current research progress of metallic materials fabricated by laser powder bed fusion process: a review, *Journal of Materials Research and Technology.* 20 (2022) 681–707. <https://doi.org/10.1016/J.JMRT.2022.07.085>.
- [37] N. Khanna, K. Zadafiya, T. Patel, Y. Kaynak, R.A. Rahman Rashid, A. Vafadar, Review on machining of additively manufactured nickel and titanium alloys, *Journal of Materials Research and Technology.* 15 (2021) 3192–3221. <https://doi.org/10.1016/J.JMRT.2021.09.088>.
- [38] J.O. Milewski, Additive Manufacturing of Metals, 258 (2017). <https://doi.org/10.1007/978-3-319-58205-4>.
- [39] G. Gong, J. Ye, Y. Chi, Z. Zhao, Z. Wang, G. Xia, X. Du, H. Tian, H. Yu, C. Chen, Research status of laser additive manufacturing for metal: a review, *Journal of Materials Research and Technology.* 15 (2021) 855–884. <https://doi.org/10.1016/J.JMRT.2021.08.050>.
- [40] I. Gibson, D. Rosen, B. Stucker, Additive manufacturing technologies: 3D printing, rapid prototyping, and direct digital manufacturing, second edition, *Additive Manufacturing Technologies: 3D Printing, Rapid Prototyping, and Direct Digital*

- Manufacturing, Second Edition. (2015) 1-498.
<https://doi.org/10.1007/978-1-4939-2113-3/COVER>.
- [41] L. Jiao, Z.Y. Chua, S.K. Moon, J. Song, G. Bi, H. Zheng, Femtosecond laser produced hydrophobic hierarchical structures on additive manufacturing parts, *Nanomaterials*. 8 (2018). <https://doi.org/10.3390/NANO8080601>.
 - [42] L. Cao, J. Li, J. Hu, H. Liu, Y. Wu, Q. Zhou, Optimization of surface roughness and dimensional accuracy in LPBF additive manufacturing, *Opt Laser Technol.* 142 (2021) 107246. <https://doi.org/10.1016/J.OPTLASTEC.2021.107246>.
 - [43] H. Shipley, D. McDonnell, M. Culleton, R. Coull, R. Lupoi, G. O'Donnell, D. Trimble, Optimisation of process parameters to address fundamental challenges during selective laser melting of Ti-6Al-4V: A review, *Int J Mach Tools Manuf.* 128 (2018) 1-20. <https://doi.org/10.1016/J.IJMACTOOLS.2018.01.003>.
 - [44] L. Dowling, J. Kennedy, D. Trimble, Effect of a modified energy density equation to achieve a more uniform energy input during LPBF for improved repeatability, *J Manuf Process.* 77 (2022) 607-615. <https://doi.org/10.1016/J.JMAPRO.2022.03.045>.
 - [45] F. Huber, M. Rasch, M. Schmidt, metals Laser Powder Bed Fusion (PBF-LB/M) Process Strategies for In-Situ Alloy Formation with High-Melting Elements, (2021). <https://doi.org/10.3390/met11020336>.
 - [46] F. Caiazzo, V. Alfieri, G. Casalino, On the Relevance of volumetric energy density in the investigation of inconel 718 laser powder bed fusion, *Materials.* 13 (2020). <https://doi.org/10.3390/MA13030538>.
 - [47] B.B. Ravichander, K. Mamidi, V. Rajendran, B. Farhang, A. Ganesh-Ram, M. Hanumantha, N. Shayesteh Moghaddam, A.

- Amerinatanzi, Experimental investigation of laser scan strategy on the microstructure and properties of Inconel 718 parts fabricated by laser powder bed fusion, Mater Charact. 186 (2022) 111765. <https://doi.org/10.1016/J.MATCHAR.2022.111765>.
- [48] D. Manfredi, F. Calignano, M. Krishnan, R. Canali, E.P. Ambrosio, S. Bihamino, D. Ugues, M. Pavese, P. Fino, Additive Manufacturing of Al Alloys and Aluminium Matrix Composites (AMCs), Light Metal Alloys Applications. (2014). <https://doi.org/10.5772/58534>.
- [49] L.N. Carter, C. Martin, P.J. Withers, M.M. Attallah, The influence of the laser scan strategy on grain structure and cracking behaviour in SLM powder-bed fabricated nickel superalloy, J Alloys Compd. 615 (2014) 338–347. <https://doi.org/10.1016/J.JALLOCOM.2014.06.172>.
- [50] Y. Lu, S. Wu, Y. Gan, T. Huang, C. Yang, L. Junjie, J. Lin, Study on the microstructure, mechanical property and residual stress of SLM Inconel-718 alloy manufactured by differing island scanning strategy, Opt Laser Technol. 75 (2015) 197–206. <https://doi.org/10.1016/j.optlastec.2015.07.009>.
- [51] M.C. Lam, S.C.V. Lim, H. Song, Y. Zhu, X. Wu, A. Huang, Scanning strategy induced cracking and anisotropic weakening in grain texture of additively manufactured superalloys, Addit Manuf. 52 (2022) 102660. <https://doi.org/10.1016/J.ADDMA.2022.102660>.
- [52] G. Marchese, G. Colera, F. Calignano, M. Lorusso, S. Bihamino, P. Minetola, D. Manfredi, Characterization and Comparison of Inconel 625 Processed by Selective Laser Melting and Laser Metal Deposition**, (2016). <https://doi.org/10.1002/adem.201600635>.
- [53] M.J. Paul, Q. Liu, J.P. Best, X. Li, J.J. Kruzic, U. Ramamurty, B. Gludovatz, Fracture resistance of AlSi10Mg fabricated by laser powder bed fusion, Acta Mater. 211 (2021) 116869. <https://doi.org/10.1016/J.ACTAMAT.2021.116869>.

- [54] L. Zhao, L. Song, J.G. Santos Macías, Y. Zhu, M. Huang, A. Simar, Z. Li, Review on the correlation between microstructure and mechanical performance for laser powder bed fusion AlSi10Mg, Addit Manuf. 56 (2022) 102914. <https://doi.org/10.1016/J.ADDMA.2022.102914>.
- [55] J.J. Marattukalam, D. Karlsson, V. Pacheco, P. Beran, U. Wiklund, U. Jansson, B. Hjörvarsson, M. Sahlberg, The effect of laser scanning strategies on texture, mechanical properties, and site-specific grain orientation in selective laser melted 316L SS, Mater Des. 193 (2020) 108852. <https://doi.org/10.1016/J.MATDES.2020.108852>.
- [56] D. Svetlizky, M. Das, B. Zheng, A.L. Vyatskikh, S. Bose, A. Bandyopadhyay, J.M. Schoenung, E.J. Lavernia, N. Eliaz, Directed energy deposition (DED) additive manufacturing: Physical characteristics, defects, challenges and applications | Enhanced Reader, (n.d.). <https://doi.org/10.1016/j.mattod.2021.03.020>.
- [57] Y. Hu, Y. Li, W. Fan, X. Gao, Q. Zhang, Q. Wang, W. Li, X. Lin, W. Huang, Hot workability and microstructural evolution of a nickel-based superalloy fabricated by laser-based directed energy deposition, J Alloys Compd. (2022) 165373. <https://doi.org/10.1016/J.JALLCOM.2022.165373>.
- [58] A.N. Alagha, S. Hussain, W. Zaki, Additive manufacturing of shape memory alloys: A review with emphasis on powder bed systems, Mater Des. 204 (2021) 109654. <https://doi.org/10.1016/J.MATDES.2021.109654>.
- [59] A. Selema, M.N. Ibrahim, P. Sergeant, Metal Additive Manufacturing for Electrical Machines: Technology Review and Latest Advancements, Energies (Basel). 15 (2022). <https://doi.org/10.3390/EN15031076>.

- [60] F. Wang, S. You, D. Jiang, F. Ning, Study on sintering mechanism for extrusion-based additive manufacturing of stainless steel through molecular dynamics simulation, *Addit Manuf.* 58 (2022) 102991. <https://doi.org/10.1016/J.ADDMA.2022.102991>.
- [61] M.A. Wagner, A. Hadian, T. Sebastian, F. Clemens, T. Schweizer, M. Rodriguez-Arbaizar, E. Carreño-Morelli, R. Spolenak, Fused filament fabrication of stainless steel structures - from binder development to sintered properties, *Addit Manuf.* 49 (2022). <https://doi.org/10.1016/J.ADDMA.2021.102472>.
- [62] S. Roshchupkin, A. Kolesov, A. Tarakhovskiy, I. Tishchenko, A brief review of main ideas of metal fused filament fabrication, *Mater Today Proc.* 38 (2021) 2063–2067. <https://doi.org/10.1016/J.MATPR.2020.10.142>.
- [63] E. Hryha, D. Riabov, Metal Powder Production for Additive Manufacturing, *Encyclopedia of Materials: Metals and Alloys.* (2022) 264–271. <https://doi.org/10.1016/B978-0-12-819726-4.00089-2>.
- [64] A.B. Spierings, M. Voegtlin, T. Bauer, K. Wegener, Powder flowability characterisation methodology for powder-bed-based metal additive manufacturing, *Progress in Additive Manufacturing.* 1 (2016) 9–20. <https://doi.org/10.1007/S40964-015-0001-4/FIGURES/12>.
- [65] C. Zhong, A. Gasser, J. Kittel, K. Wissenbach, R. Poprawe, Improvement of material performance of Inconel 718 formed by high deposition-rate laser metal deposition, *Mater Des.* C (2016) 128–134. <https://doi.org/10.1016/J.MATDES.2016.03.006>.
- [66] D. Herzog, V. Seyda, E. Wycisk, C. Emmelmann, Additive manufacturing of metals, *Acta Mater.* 117 (2016) 371–392. <https://doi.org/10.1016/J.ACTAMAT.2016.07.019>.

- [67] G. Chen, S.Y. Zhao, P. Tan, J. Wang, C.S. Xiang, H.P. Tang, A comparative study of Ti-6Al-4V powders for additive manufacturing by gas atomization, plasma rotating electrode process and plasma atomization, Powder Technol. 333 (2018) 38–46. <https://doi.org/10.1016/J.POWTEC.2018.04.013>.
- [68] H.D. Carlton, A. Haboub, G.F. Gallegos, D.Y. Parkinson, A.A. MacDowell, Damage evolution and failure mechanisms in additively manufactured stainless steel, Materials Science and Engineering: A. 651 (2016) 406–414. <https://doi.org/10.1016/J.MSEA.2015.10.073>.
- [69] Q. Jia, D. Gu, Selective laser melting additive manufacturing of Inconel 718 superalloy parts: Densification, microstructure and properties, J Alloys Compd. 585 (2014) 713–721. <https://doi.org/10.1016/J.JALLOCOM.2013.09.171>.
- [70] S. Rahmati, E. Vahabli, Evaluation of analytical modeling for improvement of surface roughness of FDM test part using measurement results, The International Journal of Advanced Manufacturing Technology. 79 (2015) 823–829. <https://doi.org/10.1007/s00170-015-6879-7>.
- [71] C. Testa, Corrosion behaviour of metal alloys obtained by means of additive manufacturing, Università degli Studi di Bergamo, 2020. <https://doi.org/10.4/JQUERY-UI.MIN.JS>.
- [72] T. DebRoy, H.L. Wei, J.S. Zuback, T. Mukherjee, J.W. Elmer, J.O. Milewski, A.M. Beese, A. Wilson-Heid, A. De, W. Zhang, Additive manufacturing of metallic components – Process, structure and properties, Prog Mater Sci. (2018). <https://doi.org/10.1016/j.pmatsci.2017.10.001>.
- [73] G.K. Lewis, E. Schlienger, Practical considerations and capabilities for laser assisted direct metal deposition, Mater Des. 21 (2000) 417–423. [https://doi.org/10.1016/S0261-3069\(99\)00078-3](https://doi.org/10.1016/S0261-3069(99)00078-3).

- [74] P. Mercelis, J. Kruth, Residual stresses in selective laser sintering and selective laser melting, *Rapid Prototyp J.* 12 (2006) 254–265. <https://doi.org/10.1108/13552540610707013>.
- [75] G. Marchese, E. Bassini, M. Calandri, E.P. Ambrosio, F. Calignano, M. Lorusso, D. Manfredi, M. Pavese, S. Biamino, P. Fino, Microstructural investigation of as-fabricated and heat-treated Inconel 625 and Inconel 718 fabricated by direct metal laser sintering: contribution of Politecnico di Torino and Istituto Italiano di Tecnologia (IIT) di Torino, *Metal Powder Report.* 71 (2016) 273–278. <https://doi.org/10.1016/J.MPRP.2016.06.002>.
- [76] D. Zhang, W. Niu, X. Cao, Z. Liu, Effect of standard heat treatment on the microstructure and mechanical properties of selective laser melting manufactured Inconel 718 superalloy, *Materials Science and Engineering: A.* 644 (2015) 32–40. <https://doi.org/10.1016/J.MSEA.2015.06.021>.
- [77] Hot Isostatic Pressing | GE Additive, (n.d.). <https://www.ge.com/additive/additive-manufacturing/materials/apc-homepage/hot-isostatic-pressing> (accessed August 29, 2019).
- [78] Jr. Stephen D. Cramer and Bernard S. Covino, ed., *ASM Handbook Volume 13A: Corrosion: Fundamentals, Testing, and Protection,* (2003) 1–1135.
- [79] P. Ganesan, C.M. Renteria, J.R. Crum, Versatile Corrosion Resistance of INCONEL® alloy 625 in Various Aqueous and Chemical Processing Environments, (n.d.).
- [80] Z. Wei, T. Goehring, M. Mioduszewski, L. Luo, A. Kotrba, M. Rybarz, K. Ellinghaus, M. Pieszkalla, Failure mechanisms and modes analysis of vehicle exhaust components and systems, *Handbook of Materials Failure Analysis with Case Studies from the*

- Aerospace and Automotive Industries. (2016) 393–432.
<https://doi.org/10.1016/B978-0-12-800950-5.00018-1>.
- [81] R.A. Lorenzoni, R.P. Gasparini, A.C. dos Santos, T. de S. Luz, M.C.S. de Macêdo, A study on the intergranular corrosion and pitting resistance of Inconel 625 coating by PTA-P, <Https://Doi.Org/10.1080/1478422X.2018.1533677>. 54 (2018) 62–74. <https://doi.org/10.1080/1478422X.2018.1533677>.
- [82] ASTM International, ASTM G48-11(2020)e1: Standard Test Methods for Pitting and Crevice Corrosion Resistance of Stainless Steels and Related Alloys by Use of Ferric Chloride Solution, (2020). <https://www.astm.org/standards/g48> (accessed September 21, 2022).
- [83] S. Mccoy, B.C. Puckett, E. Hibner, High performance age-hardenable nickel alloys solve problems in sour oil and gas service, Undefined. (2002).
- [84] L.R. Davies-Smith, J.D. Lane, T. Riley, Effect of niobium on marine crevice corrosion resistance of Inconel alloy 625, <Http://Dx.Doi.Org/10.1179/000705987798271730>. 22 (2013) 90–94. <https://doi.org/10.1179/000705987798271730>.
- [85] I.J. Moore, J.I. Taylor, M.W. Tracy, M.G. Burke, E.J. Palmiere, Grain coarsening behaviour of solution annealed Alloy 625 between 600–800 °C, Materials Science and Engineering A. 682 (2017) 402–409. <https://doi.org/10.1016/J.MSEA.2016.11.060>.
- [86] G. Marchese, E. Bassini, S. Parizia, D. Manfredi, D. Ugues, M. Lombardi, P. Fino, S. Biamino, Role of the chemical homogenization on the microstructural and mechanical evolution of prolonged heat-treated laser powder bed fused Inconel 625, Materials Science and Engineering: A. 796 (2020) 140007. <https://doi.org/10.1016/J.MSEA.2020.140007>.

- [87] Y.L. Hu, Y.L. Li, S.Y. Zhang, X. Lin, Z.H. Wang, W.D. Huang, Effect of solution temperature on static recrystallization and ductility of Inconel 625 superalloy fabricated by directed energy deposition, Materials Science and Engineering A. 772 (2020). <https://doi.org/10.1016/J.MSEA.2019.138711>.
- [88] Q. Guo, Y. Li, J. Qian, H. Yu, C. Chen, Study of the pitting corrosion at welding joints of Inconel 625 alloy under high temperature and high H₂S/CO₂ partial pressure, Int. J. Electrochem. Sci. 12 (2017) 8929–8943. <https://doi.org/10.20964/2017.10.46>.
- [89] M. Cabrini, S. Lorenzi, C. Testa, F. Brevi, S. Bihamino, P. Fino, D. Manfredi, G. Marchese, F. Calignano, T. Pastore, Microstructure and Selective Corrosion of Alloy 625 Obtained by Means of Laser Powder Bed Fusion, Materials 2019, Vol. 12, Page 1742. 12 (2019) 1742. <https://doi.org/10.3390/MA12111742>.
- [90] J.M. Costa, E.W. Sequeiros, M.T. Vieira, M.F. Vieira, Additive manufacturing: Material extrusion of metallic parts, U.Porto Journal of Engineering. 7 (2021) 53–69. https://doi.org/10.24840/2183-6493_007.003_0005.
- [91] D. Thomas, A. Gleadall, Advanced metal transfer additive manufacturing of high temperature turbine blades, International Journal of Advanced Manufacturing Technology. 120 (2022) 6325–6335. <https://doi.org/10.1007/S00170-022-09176-2>.
- [92] Material datasheet Inconel 625, (n.d.). <https://static.markforged.com/downloads/Inconel-625.pdf>.
- [93] ASTM International, ASTM B446-19: Standard Specification for Nickel-Chromium-Molybdenum-Columbium Alloy (UNS N06625), Nickel-Chromium-Molybdenum-Silicon Alloy (UNS N06219), and Nickel-Chromium-Molybdenum-Tungsten Alloy (UNS N06650) Rod and Bar, (2019). <https://www.astm.org/b0446-19.html>.

- [94] ASTM International, ASTM G28-02(2015): Standard Test Methods for Detecting Susceptibility to Intergranular Corrosion in Wrought, Nickel-Rich, Chromium-Bearing Alloys, (2016). <https://www.astm.org/g0028-02r15.html>.
- [95] ASTM International, ASTM G5-14(2021): Standard Reference Test Method for Making Potentiodynamic Anodic Polarization Measurements, (2021). <https://www.astm.org/g0005-14r21.html>.
- [96] A. Gamon, E. Arrieta, P.R. Gradi, C. Katsarelis, L.E. Murr, R.B. Wicker, F. Medina, Microstructure and hardness comparison of as-built inconel 625 alloy following various additive manufacturing processes, Results in Materials. 12 (2021). <https://doi.org/10.1016/J.RINMA.2021.100239>.
- [97] M. Fujishima, Y. Oda, R. Ashida, K. Takezawa, M. Kondo, Study on factors for pores and cladding shape in the deposition processes of Inconel 625 by the directed energy deposition (DED) method, CIRP J Manuf Sci Technol. 19 (2017) 200–204. <https://doi.org/10.1016/J.CIRPJ.2017.04.003>.
- [98] A. Evangeline, P. Sathiya, Structure–Property relationships of Inconel 625 Cladding on AISI 316L substrate produced by Hot Wire (HW) TIG metal deposition technique, Mater Res Express. 6 (2019) 106539. <https://doi.org/10.1088/2053-1591/AB350F>.
- [99] H. Wong, & K. Dawson, G.A. Ravi, L. Howlett, R.O. Jones, C.J. Sutcliffe, Multi-Laser Powder Bed Fusion Benchmarking-Initial Trials with Inconel 625, (n.d.). <https://doi.org/10.1007/s00170-019-04417-3>.
- [100] J.-R. Poulin, V. Brailovski, P. Terriault, Long fatigue crack propagation behavior of Inconel 625 processed by laser powder bed fusion: Influence of build orientation and post-processing

- conditions, (2018).
<https://doi.org/10.1016/j.ijfatigue.2018.07.008>.
- [101] J.R. Poulin, A. Kreitcberg, V. Brailovski, Effect of hot isostatic pressing of laser powder bed fused Inconel 625 with purposely induced defects on the residual porosity and fatigue crack propagation behavior, *Addit. Manuf.* 47 (2021).
<https://doi.org/10.1016/J.ADDMA.2021.102324>.
- [102] G. Sander, J. Tan, P. Balan, O. Gharbi, D.R. Feenstra, L. Singer, S. Thomas, R.G. Kelly, J.R. Scully, N. Birbilis, Corrosion of Additively Manufactured Alloys: A Review, (2018).
<https://doi.org/10.5006/2926>.
- [103] Z. Tian, C. Zhang, D. Wang, W. Liu, X. Fang, D. Wellmann, Y. Zhao, Y. Tian, A review on laser powder bed fusion of inconel 625 nickel-based alloy, *Applied Sciences*. 10 (2019) 81.
- [104] M. Rombouts, G. Maes, M. Mertens, W. Hendrix, Laser metal deposition of Inconel 625: Microstructure and mechanical properties, *J Laser Appl.* 24 (2012) 052007.
- [105] Y. Wang, X. Chen, Q. Shen, C. Su, Y. Zhang, S. Jayalakshmi, R.A. Singh, Effect of magnetic Field on the microstructure and mechanical properties of inconel 625 superalloy fabricated by wire arc additive manufacturing, *J Manuf Process.* 64 (2021) 10-19.
- [106] Y. Gao, Y. Ding, Y. Ma, J. Chen, X. Wang, J. Xu, Evolution of annealing twins in Inconel 625 alloy during tensile loading, *Materials Science and Engineering: A*. 831 (2022) 142188.
- [107] G. de Leon Nope, G. Wang, J.M. Alvarado-Orozco, B. Gleeson, Role of Elemental Segregation on the Oxidation Behavior of Additively Manufactured Alloy 625, *JOM*. 74 (2022) 1698–1706.

- [108] G. Marchese, S. Parizia, M. Rashidi, A. Saboori, D. Manfredi, D. Ugués, M. Lombardi, E. Hryha, S. Biamino, The role of texturing and microstructure evolution on the tensile behavior of heat-treated Inconel 625 produced via laser powder bed fusion, *Materials Science and Engineering A*. 769 (2020) 138500. <https://doi.org/10.1016/j.msea.2019.138500>.
- [109] G. Marchese, M. Lorusso, S. Parizia, E. Bassini, J.W. Lee, F. Calignano, D. Manfredi, M. Terner, H.U. Hong, D. Ugués, M. Lombardi, S. Biamino, Influence of heat treatments on microstructure evolution and mechanical properties of Inconel 625 processed by laser powder bed fusion, *Materials Science and Engineering A*. 729 (2018) 64–75. <https://doi.org/10.1016/j.msea.2018.05.044>.
- [110] T.E. Abioye, P.K. Farayibi, A.T. Clare, A comparative study of Inconel 625 laser cladding by wire and powder feedstock, *Materials and Manufacturing Processes*. 32 (2017) 1653–1659. <https://doi.org/10.1080/10426914.2017.1317787>.
- [111] W. Yangfan, C. Xizhang, S. Chuanchu, Microstructure and mechanical properties of Inconel 625 fabricated by wire-arc additive manufacturing, *Surf Coat Technol.* 374 (2019) 116–123. <https://doi.org/10.1016/j.surfcoat.2019.05.079>.
- [112] J. Huebner, D. Kata, J. Kusiński, P. Rutkowski, J. Lis, Microstructure of laser cladded carbide reinforced Inconel 625 alloy for turbine blade application, *Ceram Int.* 43 (2017) 8677–8684. <https://doi.org/10.1016/J.CERAMINT.2017.03.194>.
- [113] S. Lorenzi, M. Cabrini, F. Carugo, T. Pastore, Study of CO₂ condense corrosion, *Metallurgia Italiana*. 114 (2022) 52–56.
- [114] S. Lorenzi, M. Cabrini, F. Carugo, T. Pastore, Study of CO₂ condense corrosion | Studio della corrosione in condense sature di CO₂, *Metallurgia Italiana*. 114 (2022) 52–56.

- [115] A. Meyer, E. Daenicke, K. Horke, M. Moor, S. Müller, I. Langer, R.F. Singer, Metal injection moulding of nickel-based superalloy CM247LC*, <Http://Dx.Doi.Org/10.1080/00325899.2016.1142058>. 59 (2016) 51–56. <https://doi.org/10.1080/00325899.2016.1142058>.
- [116] Y. Thompson, K. Zissel, A. Förner, J. Gonzalez-Gutierrez, C. Kukla, S. Neumeier, P. Felfer, Metal fused filament fabrication of the nickel-base superalloy IN 718, *J Mater Sci.* 57 (2022) 9541–9555. <https://doi.org/10.1007/S10853-022-06937-Y/FIGURES/8>.
- [117] F. Yang, L. Dong, X. Hu, X. Zhou, Z. Xie, F. Fang, Effect of solution treatment temperature upon the microstructure and mechanical properties of hot rolled Inconel 625 alloy, *J Mater Sci.* 55 (n.d.). <https://doi.org/10.1007/s10853-020-04375-2>.
- [118] X.W. Li, L. Wang, J.S. Dong, L.H. Lou, Effect of Solidification Condition and Carbon Content on the Morphology of MC Carbide in Directionally Solidified Nickel-base Superalloys, *J Mater Sci Technol.* 30 (2014) 1296–1300. <https://doi.org/10.1016/J.JMST.2014.06.010>.
- [119] M. Cabrini, S. Lorenzi, C. Testa, T. Pastore, F. Brevi, S. Biamino, P. Fino, D. Manfredi, G. Marchese, F. Calignano, F. Scenini, Evaluation of Corrosion Resistance of Alloy 625 Obtained by Laser Powder Bed Fusion, *J Electrochem Soc.* 166 (2019) C3399–C3408. <https://doi.org/10.1149/2.0471911JES/XML>.
- [120] K. Lutton Cwalina, C.R. Demarest, A.Y. Gerard, J.R. Scully, Revisiting the effects of molybdenum and tungsten alloying on corrosion behavior of nickel-chromium alloys in aqueous corrosion, *Curr Opin Solid State Mater Sci.* 23 (2019) 129–141. <https://doi.org/10.1016/J.COSSMS.2019.03.002>.
- [121] G. Vieira Braga Lemos, A. Bellegard Farina, H. Piaggio, L. Bergmann, J. Zoppas Ferreira, J. Fernandez dos Santos, G. vander

- Voort, A. Reguly, Mitigating the susceptibility to intergranular corrosion of alloy 625 by friction-stir welding, (123AD). <https://doi.org/10.1038/s41598-022-07473-0>.
- [122] L. Xu, J. Zhang, Y. Han, L. Zhao, H. Jing, Insights into the intergranular corrosion of overlay welded joints of X65-Inconel 625 clad pipe and its relationship to damage penetration, Corros Sci. 160 (2019). <https://doi.org/10.1016/J.CORSCI.2019.108169>.
- [123] A. Mostafaei, J. Toman, E.L. Stevens, E.T. Hughes, Y.L. Krimer, M. Chmielus, Microstructural evolution and mechanical properties of differently heat-treated binder jet printed samples from gas-and water-atomized alloy 625 powders, Acta Mater. 124 (2017) 280-289.